Using a Two-Phase Columnar Solidification Model to Study the Principle of Mechanical Soft Reduction in Slab Casting

MENGHUAI WU, JOSEF DOMITNER, and ANDREAS LUDWIG

A two-phase columnar solidification model is used to study the principle of mechanical soft reduction (MSR) for the reduction of centerline segregation in slab casting. The two phases treated in the model are the bulk/interdendritic melt and the columnar dendrite trunk. The morphology of the columnar dendrite trunk is simplified as stepwise growing cylinders, with growth kinetics governed by the solute diffusion in the interdendritic melt around the growing cylindrical columnar trunk. The solidifying strand shell moves with a predefined velocity and the shell deforms as a result of bulging and MSR. The motion and deformation of the columnar trunks in response to bulging and MSR is modeled following the work of Miyazawa and Schwerdtfeger from the 1980s. Melt flow, driven by feeding of solidification shrinkage and by deformation of the strand shell and columnar trunks, as well as the induced macrosegregation are solved in the Eulerian frame of reference. A benchmark slab casting (9-m long, 0.215-m thick) of plain carbon steel is simulated. The MSR parameters influencing the centerline segregation are studied to gain a better understanding of the MSR process. Two mechanisms in MSR modify the centerline segregation in a slab casting: one establishes a favorable interdendritic flow field, whereas the other creates a non-divergence-free deformation of the solid dendritic skeleton in the mushy region. The MSR efficiency depends not only on the reduction amount in the slab thickness direction but also strongly on the deformation behavior in the longitudinal (casting) direction. With enhanced computation power the current model can be applied for a parameter study on the MSR efficiency of realistic continuous casting processes.

DOI: 10.1007/s11661-011-0940-4

I. INTRODUCTION

MECHANICAL soft reduction (MSR) has been shown in industrial practice to reduce centerline/axial segregation in slab and bloom castings[1–10]; however, control of the MSR process remains a trial and error process in plant operations. Empirical knowledge (Figure 1) has shown that satisfactory MSR efficiency can be achieved when MSR is positioned correctly on the strand and carried out with the appropriate reduction intensity. The MSR position is usually determined in terms of the solid fraction of the strand core (*i.e.*, the casting centerline)—the solid fraction at the start $\left(f_{\mathrm{s,Start}}^{\mathrm{cent}}\right)$ and at the end position $\left(f_{\mathrm{s,End}}^{\mathrm{cent}}\right)$ of MSR. The reduction intensity is usually defined by the reduction rate, which is the reduction amount (ε) divided by the length of the reduction segment (l_{SR}). When the MSR is performed too early, too late, or too intensely, the risk of crack formation and growth increases. According to Thome and Karste,[3] the optimum MSR is defined by the minimum intensity of reduction that is necessary to compensate shrinkage during solidification without creating internal cracks. Implementation of the aforementioned empirical knowledge in industry process is not straightforward. However, depending on the casting format and steel grade, the suggested MSR position can differ significantly from case to case (*e.g.*, between 0.2 $\left[f_{\mathrm{s,Start}}^{\mathrm{cent}}\right]$ and 0.9 $\left[f_{\mathrm{s,End}}^{\mathrm{cent}}\right]$ for higher carbon steel,[11,12] between 0.2 and 0.7 for low carbon steel,[13,14] or between 0.37 and 0.51 for a medium steel).[15] Optimum reduction rates achieved in each case were also surprisingly different (*e.g.*, between 1.8 and 6.6 mm/m[11,14] or 0.72 and 4.7 mm/m[11,15]). Given the discrepancy in optimum MSR position and reduction rate, future investigation into the MSR process is warranted to understand and improve the practical implementation of the process in industry.

Use of computational models to investigate macrosegregation in slab casting caused by bulging (mechanical shell deformation) was pioneered by Miyazawa and Schwerdtfeger in the early 1980s.[16] Despite the model simplicity, the limited computational resources available at that time, when only a small section of slab between one roll pair could be simulated, the model was the first to reveal the main mechanism of centerline macrosegregation in the slab casting. Although solidification

MENGHUAI WU, Associate Professor and Chair for Simulation and Modeling of Metallurgical Processes, Christian Doppler Laboratory for Advanced Process Simulation of Solidification and Melting, University of Leoben, A-8700 Leoben, Austria. Contact e-mail: menghuai.wu@unileoben.ac.at JOSEF DOMITNER, PhD Student, and ANDREAS LUDWIG, Professor and Chair for Simulation and Modeling of Metallurgical Processes, are with the Christian Doppler Laboratory for Multiphase Modeling of Metallurgical Processes, University of Leoben.

Manuscript submitted April 5, 2011.
Article published online October 19, 2011

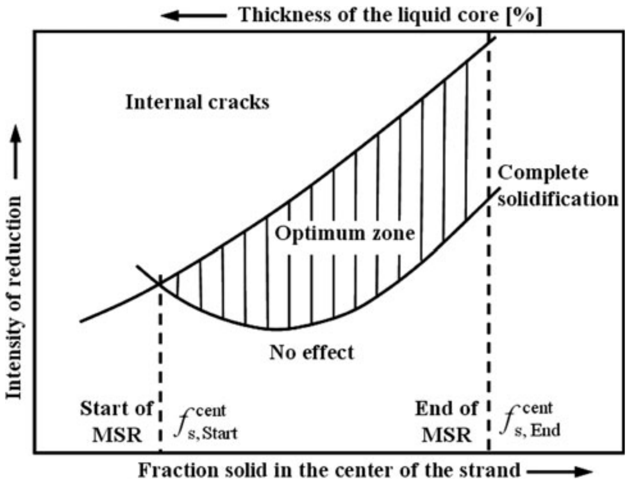

Fig. 1—Schematic of the optimum MSR zone[3].

shrinkage has a significant influence on the feeding flow in the casting direction, the bulging-induced flow component (perpendicular to casting direction) had a dominant impact on the centerline segregation. The model was later extended by Kajitani *et al.*[17] to include a more precise calculation of the mechanical deformation (bulging) between successive roll pairs, a larger calculation domain (five successive roll pairs), and the effects of soft reduction. The fundamental segregation phenomenon in the slab casting was confirmed, and the accumulated effect of segregation caused by the successive bulging roll pairs was revealed. However, modeling results on the influence of soft reduction on macrosegregation did not coincide with industry experiences. For example, it is widely accepted in industry that soft reduction reduces centerline positive segregation, whereas simulations incorporating a relatively large amount of bulging have shown that centerline positive segregation increases slightly when soft reduction is imposed in the model. As the authors stated, their model could not converge at volume fractions of solid lower than 0.2 or high than 0.7. This limitation together with other model uncertainties might be responsible for the aforementioned discrepancy between empirical knowledge and modeling results. Recently, the current authors used a two-phase columnar solidification model to study the centerline segregation of slab casting in a more realistic domain (including 100 bulging roll pairs) with improved boundary conditions.[18,19] The modeling results agreed with the findings of the previous works[16,17] for cases without soft reduction.

The current study extends this investigation on centerline segregation with the inclusion of soft reduction in the working model. A parameter study is carried out by varying the intensity and position of the MSR and the mechanical deformation behavior of the MSR segment in both slab thickness direction and casting direction. The main goal of the current study is to achieve a deeper understanding of the principle of MSR through parameter studies and to explore the potential for optimization of industry MSR processes.

II. MODEL DESCRIPTIONS

A. *Columnar Solidification*

The two-phase columnar solidification model is a simplified version of the mixed columnar-equiaxed solidification model,[20–22] in which the presence of equiaxed crystals is neglected. Conservation equations, source and exchange terms, and auxiliary equations are summarized in Table I. Details of the numerical model for columnar solidification are described elsewhere.[23] A brief outline of the model assumptions includes the following:

(a) Two phases are included in the model—the melt (bulk or interdendritic) and the columnar dendrite trunks.
(b) The morphology of the columnar dendrite trunks is approximated by step-wise cylinders, and the primary dendrite arm spacing λ_1 is constant. The arrangement of the cylindrical columnar trunks is assumed to be staggered or aligned.
(c) The columnar trunks initially grow from the casting (slab) surface when constitutional undercooling is achieved. Solidification begins in correlation with the liquidus isotherm. The columnar tip front position is assumed to be coincident with 1 pct of solid phase.
(d) The liquid-to-solid mass transfer rate $M_{\ell s}$ is calculated based on the growth velocity of the columnar trunks v_{R_c}, which is governed by the diffusion of a solute element in the interdendritic melt around each cylindrical trunk.
(e) Volume-averaged concentrations (c_ℓ, c_s) are numerical results, and macrosegregation is evaluated by the mixture concentration, c_{mix}. We assume thermodynamic equilibrium at the liquid–solid interface, which dictates the liquid–solid interface concentrations (c_ℓ^*, c_s^*). Solid back diffusion is neglected. The difference ($c_\ell^* - c_\ell$) is the driving force for growth of the columnar trunks.
(f) A linearized binary Fe-C phase diagram is used with a constant solute redistribution coefficient k and a constant liquidus slope m.
(g) Interdendritic flow resistance in the mushy zone is calculated via a permeability law according to the Blake–Kozeny approach.[24]

Steel continuous casting has an extremely long mushy region. Theoretically, solidification shrinkage of the last remaining melt, although it occurs deep in the mushy zone where the permeability is low, should also be fed. In reality, micropores form, or the deformation of the solid dendritic skeletons compensate for the solidification shrinkage of the last remaining melt so that no feeding is necessary. However, both pore formation and solid deformation are not explicitly modeled. To avoid this difficulty, a simplified porosity model (SPM) has been proposed and implemented for modeling the solidification of the last remaining melt ($f_\ell = 0.05$).[18,19] The solid phase formed from the last remaining melt is treated as a solid–pore mixture phase with a mixture density ρ_{s+p} equal to liquid density ρ_ℓ, and thus, the last remaining melt solidifies without feeding.

Table I. Conservation Equations, Source and Exchange Terms, Auxiliary Equation

Conservation equations			
Mass	$\frac{\partial}{\partial t}(f_\ell \rho_\ell) + \nabla \cdot \left(f_\ell \rho_\ell \vec{u}_\ell\right) = -M_{\ell s}$		[1]
	$\frac{\partial}{\partial t}(f_s \rho_s) + \nabla \cdot \left(f_s \rho_s \vec{u}_s\right) = M_{\ell s}$		
Momentum	$\frac{\partial}{\partial t}\left(f_\ell \rho_\ell \vec{u}_\ell\right) + \nabla \cdot \left(f_\ell \rho_\ell \vec{u}_\ell \otimes \vec{u}_\ell\right) = -f_\ell \nabla p + \nabla \cdot \bar{\bar{\tau}}_\ell + f_\ell \rho_\ell \vec{g} - \vec{U}^{M}_{\ell s} - \vec{U}^{D}_{\ell s}$		[2]
	where $\bar{\bar{\tau}}_\ell = \mu_\ell f_\ell \left(\nabla \cdot \vec{u}_\ell + \left(\nabla \cdot \vec{u}_\ell\right)^T\right)$		
Species	$\frac{\partial}{\partial t}(f_\ell \rho_\ell c_\ell) + \nabla \cdot \left(f_\ell \rho_\ell \vec{u}_\ell c_\ell\right) = -C^{M}_{\ell s} - C^{D}_{\ell s}$		[3]
	$\frac{\partial}{\partial t}(f_s \rho_s c_s) + \nabla \cdot \left(f_s \rho_s \vec{u}_s c_s\right) = C^{M}_{\ell s} + C^{D}_{\ell s}$		
Enthalpy	$\frac{\partial}{\partial t}(f_\ell \rho_\ell h_\ell) + \nabla \cdot \left(f_\ell \rho_\ell \vec{u}_\ell h_\ell\right) = \nabla \cdot (f_\ell k_\ell \nabla \cdot T_\ell) + Q^{M}_{\ell} - Q^{D}_{\ell s}$		[4]
	$\frac{\partial}{\partial t}(f_s \rho_s h_s) + \nabla \cdot \left(f_s \rho_s \vec{u}_s h_s\right) = \nabla \cdot (f_s k_s \nabla \cdot T_s) + Q^{M}_{s} + Q^{D}_{\ell s}$		
	where $h_\ell = \int_{T_{ref}}^{T_\ell} c^{\ell}_{p} dT + h^{ref}_{\ell}$ and $h_s = \int_{T_{ref}}^{T_s} c^{s}_{p} dT + h^{ref}_{s}$		
Solidification net mass transfer			
Mass transfer	$M_{\ell s} = v_{R_c} \cdot S_A \cdot \rho_s \cdot \Phi_{imp}$		[5]
Col. trunk growth velocity	$v_{R_c} = \frac{dR_c}{dt} = \frac{D_\ell}{R_c} \cdot \frac{(c^*_\ell - c_\ell)}{(c^*_\ell - c^*_s)} \cdot \ln^{-1}\left(\frac{R_f}{R_c}\right)$		[6]
Arrangement of col. trunks	Staggered	Aligned	
Diameter of col. trunks	$d_c (= 2R_c) = \lambda_1 \cdot \sqrt{\frac{\sqrt{12} \cdot f_s}{\pi}}$	$d_c (= 2R_c) = 2\lambda_1 \cdot \sqrt{\frac{f_s}{\pi}}$	[7]
Far field radius of col. trunks	$R_f = \frac{1}{\sqrt{3}} \cdot \lambda_1$	$R_f = \frac{\sqrt{2}}{2} \cdot \lambda_1$	[8]
Col. surface concentration	$S_A = \frac{2 \cdot d_c \cdot \pi}{\sqrt{3} \cdot \lambda_1^2}$	$S_A = \frac{\pi \cdot d_c}{\lambda_1^2}$	[9]
Growing surface impingement	$\Phi_{imp} = \begin{cases} 1 & d_c \le \lambda_1 \\ 2\sqrt{3} \cdot f_\ell / (2\sqrt{3} - \pi) & d_c > \lambda_1 \end{cases}$	$\Phi_{imp} = \begin{cases} 1 & d_c \le \lambda_1 \\ 4 f_\ell / (4 - \pi) & d_c > \lambda_1 \end{cases}$	[10]
Source and exchange terms			
Momentum transfer	$\vec{U}^{M}_{\ell s} = \begin{cases} \vec{u}_\ell \cdot M_{\ell s} & \text{solidification} \\ \vec{u}_s \cdot M_{\ell s} & \text{melting} \end{cases}$	$\vec{U}^{D}_{\ell s} = \frac{f_\ell^2 \cdot \mu_\ell}{K} \cdot (\vec{u}_\ell - \vec{u}_s)$ where $K = 6 \times 10^{-4} \cdot \lambda_1^2 \cdot \frac{f_\ell^3}{(1 - f_\ell)^2}$	[11]
Species transfer	$C^{M}_{\ell s} = \begin{cases} k \cdot c^*_\ell \cdot M_{\ell s} & \text{solidification} \\ c_s \cdot M_{\ell s} & \text{melting} \end{cases}$	$C^{D}_{\ell s}$ neglected	[12]
Enthalpy transfer and latent heat	$Q^{M}_{\ell} = (\Delta h_f \cdot f_\ell - h_\ell) \cdot M_{\ell s}$	$Q^{D}_{\ell s} = H^* \cdot (T_\ell - T_s)$	[13]
	$Q^{M}_{s} = (\Delta h_f \cdot f_s + h_s) \cdot M_{\ell s}$	where $H^* = 10^9$ Wm^{-2}K^{-1}	
Auxiliary equation			
Mixture concentration	$c_{mix} = (c_\ell \cdot \rho_\ell \cdot f_\ell + c_s \cdot \rho_s \cdot f_s)/(\rho_\ell \cdot f_\ell + \rho_s \cdot f_s)$		[14]

B. *Mechanical Deformation Due to Bulging*

In the current model, the moving velocity of the solidified shell, and the deformation of the growing dendrites are modeled following the work of Miyazawa and Schwerdtfeger[16]; a thermal mechanical model is not implemented. The following divergence-free condition is applied for the fully solidified domain:

$$\nabla \cdot \vec{u}_s = 0 \qquad [15]$$

As schematically shown in Figure 2(a), a two-dimensional (2D) scenario is considered. The z-component (casting direction) of solid velocity $u_{z,s}$ is assumed to be constant, and equal to the casting speed v_{cast}. For the fully solidified strand shell, the x-component of solid velocity $u_{x,s}$ is assumed to be equal to the surface velocity $u^{b}_{x,s}$. The surface velocity of the strand shell can be derived according to the predefined bulging profile of the geometry. With the previous assumptions, the divergence-free condition of the fully solidified shell (Eq. [15]) is fulfilled. In the mushy zone, two regions, designated A and B, are distinguished. In region A, where the strand shells go apart because of bulging, the solid velocity x-component $u_{x,s}$ is constant and equal to the surface velocity of the shell $u^{b}_{x,s}$. In region B, where the strand shells are pressed together, $u_{x,s}$ is linearly reduced from the maximum in the solidus isoline (assumed to be fully solidified)

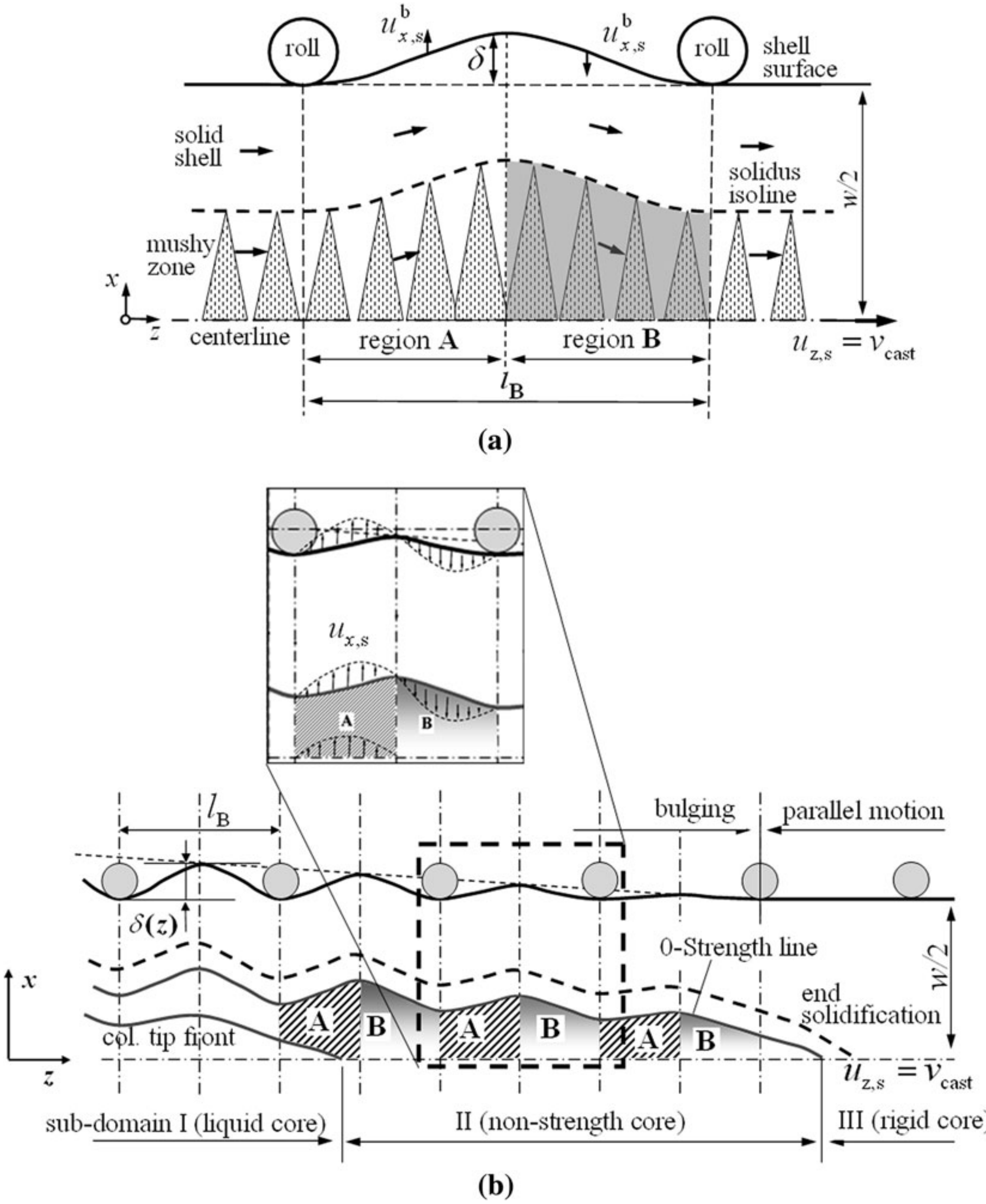

Fig. 2—Schematic of the motion of the solid shell and growing dendrites in the two-phase region (*a*) between one pair of rolls, reproduced from literature[16]; (*b*) between a series of bulging roll pairs.

to zero at the casting center, and is expressed as follows:

$$u_{x,s} = u_{x,s}^{b} \cdot \frac{f_s - f_s^{cent}}{1 - f_s^{cent}} \qquad [16]$$

where f_s^{cent} is the solid volume fraction at the casting centerline. This linear velocity reduction mimics deformation within the partially solidified strand when the dendrites are pressed together. In this region, the divergence-free condition will not be fulfilled for the solid phase.

The previous model description is implemented with necessary extensions to treat multiple bulging roll pairs, as shown in Figure 2(b). The z-component of solid velocity $u_{z,s}$ is still considered constant and equal to the casting speed v_{cast}. For the x-component of the solid velocity $u_{x,s}$, a more sophisticated treatment must be considered. For the fully solidified strand shell, the x-component of solid velocity $u_{x,s}$ is assumed to be equal to the surface velocity $u_{x,s}^{b}$. The mushy zone is divided into the following subdomains according to the state of the solidification at the casting centerline: subdomain I with a liquid core in the casting center ($f_s^{cent} \leq 0.01$), subdomain II with a nonstrength core in the casting center ($0.01 < f_s^{cent} \le f_s^{0-strength}$), and subdomain III with rigid core in the casting center ($f_s^{cent} > f_s^{0-strength}$). In subdomain I, where the dendrite tips have not met at the centerline, it is still assumed that the solid dendrites move with the same velocity as that of the fully solidified strand shell. In subdomain III, the velocity is $u_x = 0$. The bulging stops before subdomain III begins. In subdomain II, where the columnar tip fronts meet at the centerline, regions A and B are distinguished. In region A, the solid velocity x-component $u_{x,s}$ is equal to the surface velocity of the shell $u^b_{x,s}$. In region B, $|u_{x,s}|$ is reduced from its maximum at a 0-strength isoline ($f_s^{0-strength}$) to zero at the casting center. We believe that it is more likely that the most deformation happens near the strand core where the solid volume fraction is lowest rather than a homogenous deformation across the whole section of the mushy zone. The following modification to Eq. [16] is suggested:

$$u_{x,s} = u^b_{x,s} - u^b_{x,s} \cdot e^{-\phi_1 \cdot \frac{(f_s - f_s^{cent})}{\left(f_s^{0-strength} - f_s\right)^{\phi_2}}} \quad [17]$$

where the constants $\phi_1 = 50$ and $\phi_2 = 0.25$ were chosen to ensure that the most dendrite deformation occurs near the casting centerline where the solid fraction is lowest.[19]

The positions of the columnar tip front, 0-strength isoline, and the end of solidification (Figure 2(b)) are calculated by the model. The columnar tip front is assumed to coincide with $f_s = 0.01$. According to industrial data, the 0-strength isoline coincides with a solid fraction of 0.8.[18,19] The end of solidification is defined at the position where the SPM model is "switched on," and it coincides with $f_s = 0.95$.

C. *Mechanical Deformation Caused by Soft Reduction*

Deformation of the solid phase in the MSR segment is considered in 2D (Figure 3), and the deformation of the strand in the third dimension (slab-width direction) is neglected. In the MSR segment, the strand can be pressed in the thickness direction, and the strand can also stretch (elongate) or be shortened in the longitudinal (casting) direction. The divergence-free condition ($\nabla \cdot \vec{u}_s = 0$) applies in the region where the solid phase is considered noncompressible (*i.e.*, the solid fraction is higher than $f_s^{0-strength}$). A non-divergence-free condition ($\nabla \cdot \vec{u}_s = 0$) applies in the mushy zone, where solid fraction is smaller than $f_s^{0-strength}$. Whether the volume of the strand is in compression or expansion in the MSR segment is determined according to the mechanical deformation behavior in both thickness and longitudinal (casting) directions. The deformation in the thickness direction is quantified by the reduction amount ε, whereas the deformation in the longitudinal direction is quantified according to the velocities of the solid phase at the entrance and exit of the MSR segment $u^{IN}_{z,s}$ and $u^{OUT}_{z,s}$. Here $u^{IN}_{z,s}$ is equal to casting velocity v_{cast}. $u^{OUT}_{z,s}$ can be equal to or different from $u^{IN}_{z,s}$, depending on the deformation behavior of the MSR segment. The section thickness of the strand is $w/2$ at the entrance of the soft-reduction segment and $w/2 - \varepsilon$ at the exit. With a given $u^{IN}_{z,s}$, $u^{OUT}_{z,s}$, w, ε, and l_{SR}, we define the following MSR factor:

$$\gamma = \left(u^{OUT}_{z,s} \cdot (w - 2\varepsilon) - u^{IN}_{z,s} \cdot w\right) \cdot \frac{1}{w l_{SR}} \quad [18]$$

The MSR factorγ has the same sign and same unit as $\nabla \cdot \vec{u}_s = 0$, and it can be understood as a volume averaged divergence of the solid velocity over the entire MSR segment. A zero value of γ indicates that a divergence-free condition for the solid phase applies to the whole soft-reduction segment, including the fully solidified region and mushy zone. A negative γ means that the volume of the MSR segment is compressed, and that more solid phase is entering rather than leaving the segment (not including the solidification in the MSR segment), corresponding to a scenario of $\nabla \cdot \vec{u}_s < 0$. As the region with a solid fraction larger than $f_s^{0-strength}$ is not compressible, the volume compression occurs in the mushy zone where the solid volume fraction is lower. In other words, the interdendritic space between dendrites in the mushy zone is reduced (*i.e.*, the dendritic skeleton is compressed and the interdendritic melt is squeezed out of the interdendritic space). A positive γ, corresponding to $\nabla \cdot \vec{u}_s < 0$, means that the interdendritic space in the lower solid fraction region is enlarged and the melt elsewhere will be drawn into the segment to feed the enlarged interdendritic space.

For clarity, the following terminologies are strictly distinguished. The one-dimensional (1D) deformation of the strand in the thickness direction is referred to as

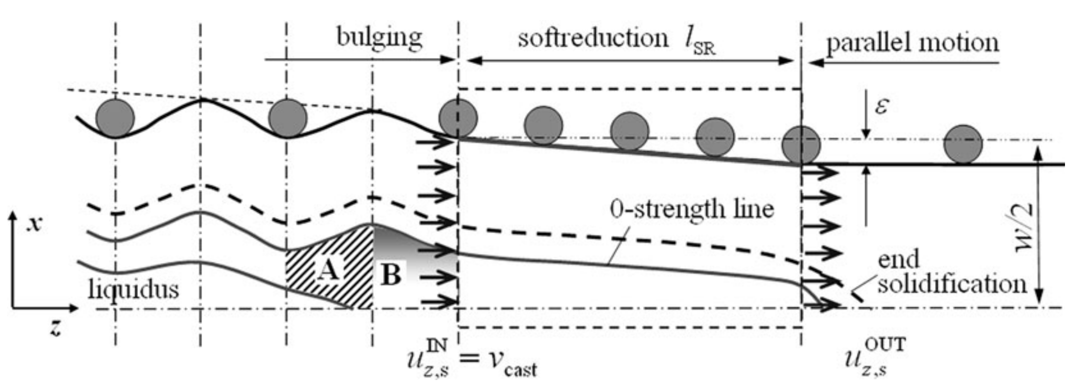

Fig. 3—Schematic of soft-reduction segment.

"reduction," quantified by ε. The 1D deformation of the strand in longitudinal direction is referred to as "elongation" or "shortening," quantified according to $u_{z,s}^{\mathrm{IN}}$ and $u_{z,s}^{\mathrm{OUT}}$ of the MSR segment. The general volume deformation of the MSR segment is referred to as volume "compression" or "expansion," quantified by γ.

As shown in Figure 3, we assume no bulging between the roll pair in the soft-reduction segment. The surface profile of the strand shell in the soft-reduction segment is linear, as shown in the following equation:

$$x^{\mathrm{b}}(z) = \frac{w}{2} - \frac{\varepsilon}{l_{\mathrm{SR}}} \cdot (z - z_1) \qquad [19]$$

where z_1 is the coordinate of the start position of the MSR segment.

The z-component of the solid velocity $u_{z,s}$ in the MSR segment (including the slab surface $u_{z,s}^{\mathrm{b}}$) is assumed, by the following equation, to be linear:

$$u_{z,s}^{\mathrm{b}} = u_{z,s} = v_{\mathrm{cast}} + \frac{u_{z,s}^{\mathrm{OUT}} - v_{\mathrm{cast}}}{l_{\mathrm{SR}}} \cdot (z - z_1) \qquad [20]$$

We know that the x-component of the surface velocity of the moving strand is calculated by $u_{x,s}^{\mathrm{b}} = u_{z,s}^{\mathrm{b}} \cdot \frac{dx^{\mathrm{b}}(z)}{dz}$; hence, the following is true:

$$u_{x,s}^{\mathrm{b}} = -\left(v_{\mathrm{cast}} + \frac{u_{z,s}^{\mathrm{OUT}} - v_{\mathrm{cast}}}{l_{\mathrm{SR}}} \cdot (z - z_1)\right) \cdot \frac{\varepsilon}{l_{\mathrm{SR}}} \qquad [21]$$

In the domain of the MSR segment, when the solid fraction is larger than $f_s^{0-\mathrm{strength}}$, the following divergence-free condition is applied $\nabla \cdot \vec{u}_s = 0$, that is:

$$\frac{\partial u_{x,s}}{\partial x} = -\frac{u_{z,s}^{\mathrm{OUT}} - v_{\mathrm{cast}}}{l_{\mathrm{SR}}} \qquad [22]$$

Integration of Eq. [22] with respect to x results in the following equation:

$$u_{x,s} = A - \left(\frac{u_{z,s}^{\mathrm{OUT}} - v_{\mathrm{cast}}}{l_{\mathrm{SR}}}\right) \cdot x \qquad [23]$$

The integral constant A can be obtained as follows by applying boundary condition $u_{x,s} = u_{x,s}^{\mathrm{b}}$ at the strand surface, $x = x^{\mathrm{b}}(z)$:

$$A = \left(\frac{u_{z,s}^{\mathrm{OUT}} - v_{\mathrm{cast}}}{l_{\mathrm{SR}}}\right) \cdot \left(\frac{w}{2} - \frac{2\varepsilon}{l_{\mathrm{SR}}} \cdot (z - z_1)\right) - v_{\mathrm{cast}} \cdot \frac{\varepsilon}{l_{\mathrm{SR}}} \qquad [24]$$

Equation [23] is used to calculate the solid velocity of the strand shell where the solid volume fraction is larger than $f_s^{0-\mathrm{strength}}$. At the position of the $f_s^{0-\mathrm{strength}}$isoline, if the calculated $u_{x,s}$ from Eq. [23] is positive, then the columnar dendrite trunks that connect to this position move up with the solidified strand shell. If the calculated $u_{x,s}$ at the position of $f_s^{0-\mathrm{strength}}$isoline is negative, then the columnar dendrite trunks that connect to this position deform and $u_{x,s}$ decreases from its maximum velocity at the 0-strength isoline to zero at the casting centerline according to Eq. [17].

III. CONFIGURATION OF THE BENCHMARK SLAB AND MODEL SETUP

A 2D benchmark slab casting of plain carbon steel (Fe-0.18 wt pct C) was simulated. As shown in Figure 4,

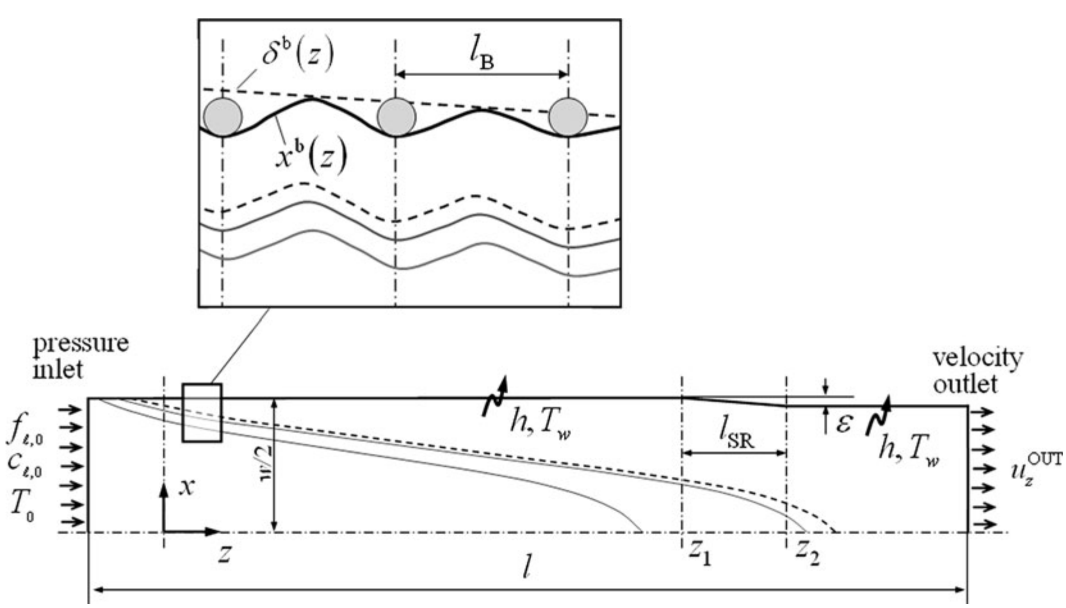

Fig. 4—Configuration of the benchmark slab casting.

the surface profile caused by bulging is described by the following equation:

$$x^{\mathrm{b}}(z) = \frac{w}{2} + \frac{\delta^{\mathrm{b}}(z)}{2} + \frac{\delta^{\mathrm{b}}(z)}{2} \cdot \sin\left(2\pi \frac{z - z_0}{l_{\mathrm{B}}} - \frac{\pi}{2}\right) \quad [25]$$

where $\delta^{\mathrm{b}}(z) = \delta^{\mathrm{b}}_{\mathrm{max}} + \frac{\delta^{\mathrm{b}}_{\mathrm{max}}}{l_{\mathrm{B}} N} \cdot (z_0 - z)$.

The slab is assumed to be cast horizontally. The hot melt enters through the inlet (left), and the solid strand is continuously drawn from the outlet (right). The melt solidifies as it passes through the domain; thus, a constant velocity boundary condition u_z^{OUT} $(= u^{\mathrm{OUT}}_{z,\ell} = u^{\mathrm{OUT}}_{z,\mathrm{s}})$ is applied at the outlet, and a pressure boundary condition is applied at the inlet. The heat-transfer boundary condition and the casting speed are applied so that full solidification can be achieved within the calculation domain when a steady-state condition is reached. To facilitate the parameter study of the influence of MSR position on the centerline segregation, a so-called "modified heat capacity method" from Niyama *et al.*[25] is used to "adjust" the end solidification at the desired position instead of changing the MSR position from the benchmark geometry. All the parameters used for the process simulations are listed in Table II.

Table II. Parameters Used for the Process Simulations

Thermophysical properties:	Thermodynamic parameters:
$\mu_\ell = 5.6 \times 10^{-3}$ kg m^{-1} s^{-1}	$c_{\mathrm{E}} = 4.3$ wt pct
$c_{\mathrm{p}}^{\ell}\left(c_{\mathrm{p}}^{\mathrm{s}}\right) = 808.25$ J kg^{-1} K^{-1}	$k = 0.36$
$D_\ell = 2 \times 10^{-8}$ m^2 s^{-1}	$m = -116.7.0$ K/wt pct
$k_\ell = 29$ W m^{-1} K^{-1}	$T_{\mathrm{f}} = 1811.0$ K (1538 °C)
$k_s = 35$ W m^{-1} K^{-1}	$\Delta h_f = 2.56 \times 10^5$ J kg^{-1}
$\rho_\ell = 7027$ kg m^{-3}	
$\rho_{\mathrm{s}} = 7324$ kg m^{-3}	
Soft reduction parameters*:	**Slab geometry:**
$z_1 = 4.5$ m $z_2 = 6.0$ m	$l = 9$ m
$l_{\mathrm{SR}} = 1.5$ m $\varepsilon = 2 \times 10^{-4}$ m	$w = 0.215$ m
Number of roll pairs and bulging parameters:	**Boundary conditions*:**
	$c_{\ell,0} = 0.18$ wt pct
$N = 100$	$f_{\ell,0} = 1 - 10^{-5}$
$\delta^{\mathrm{b}}_{\mathrm{max}} = 8 \times 10^{-4}$ m	$h = 235$ W m^{-2} K^{-1}
$l_{\mathrm{B}} = 0.06$ m	$T_0 = 1791$ K (1518 °C)
$z_0 = 0.0$ m	$T_{\mathrm{w}} = 325$ K (52 °C)
	$v_{\mathrm{cast}} = 6.0 \times 10^{-3}$ m s^{-1}
	$u_z^{\mathrm{OUT}} = 6.02241 \times 10^{-3}$ m s^{-1}

*Values are varied in the parameter study.

With this benchmark geometry, a study was carried out by varying the MSR parameters, as listed in Table III. In Case 1, no soft reduction was observed. From Cases 2 through 7, the same reduction amount ε and reduction length l_{SR} are used, but the reduction position $f^{\mathrm{cent}}_{\mathrm{s,Start}}$ and the MSR factor γ are varied. From Cases 8 through 12, a so-called "flattening" process is simulated. The reduction amount ε is set to zero, but the starting position of flattening is varied. As mentioned previously, the variation of the MSR position is achieved by adjusting the end solidification through a "modified heat capacity method."[25] The significant modeling results are also listed in Table III, but are discussed later.

The solidification model is developed within the framework of the CFD software package, FLUENT (Fluent Inc. Canonsburg, PA).[20–23,26] The FLUENT formulation is fully implicit; hence, the highly nonlinear governing equations must be solved iteratively. Although only the final steady-state solution is sought, the calculations are carried out transiently. The initial condition of the calculation domain is set as the same as the inlet boundary condition (T_0, $c_{\ell,0}$, and $f_{\ell,0}$). That is, the whole domain is initially filled with liquid melt, begins to cool down, and solidifies from the surface until the columnar tip front meets at the casting center and steady-state is achieved. During solidification, the solidified phase is pulled toward the outlet direction with the predefined velocity (Sections II–B through II–C).

Table III. Parameter Study for the Soft Reduction

	MSR Parameters				$c_{\mathrm{mix}} (\times 10^{-4})$			
	l_{SR}(m)	ε(mm)	γ ($\times 10^{-6}$)	$f^{\mathrm{cent}}_{\mathrm{s,Start}}$	min	max	Δc_{mix}	Grade*
Case 1	0	0	0	—	17.4	18.8	1.4	X
Case 2	1.5	0.2	−7.44	0.4	16.2	18.2	2.0	XX
Case 3	1.5	0.2	8.52	0.4	17.3	18.8	1.5	X
Case 4	1.5	0.2	0	0.4	17.2	18.0	0.8	✔
Case 5	1.5	0.2	−15.44	0.4	15.3	18.5	3.2	XX
Case 6	1.5	0.2	4.52	0.2	17.2	18.0	0.8	✔
Case 7	1.5	0.2	8.52	0.2	17.4	18.2	0.8	✔
Case 8	—	0	0	0.5	16.7	18.7	2.0	XX
Case 9	—	0	0	0.4	17.2	18.0	0.8	✔
Case 10	—	0	0	0.2	17.3	18.0	0.7	✔
Case 11	—	0	0	0.1	17.4	18.0	0.6	✔
Case 12	—	0	0	0.01	17.4	18.0	0.6	✔

*The soft reduction efficiency is graded according to Δc_{mix}. When $\Delta c_{\mathrm{mix}} \geq 2.0 \times 10^{-4}$, it is graded as very bad (XX); $2.0 \times 10^{-4} > \Delta c_{\mathrm{mix}} \geq 1.0 \times 10^{-4}$, bad (X); $1.0 \times 10^{-4} > \Delta c_{\mathrm{mix}} \geq 0.5 \times 10^{-4}$, good (✔); $0.5 \times 10^{-4} > \Delta c_{\mathrm{mix}} \geq 0.0$, very good (✔✔).

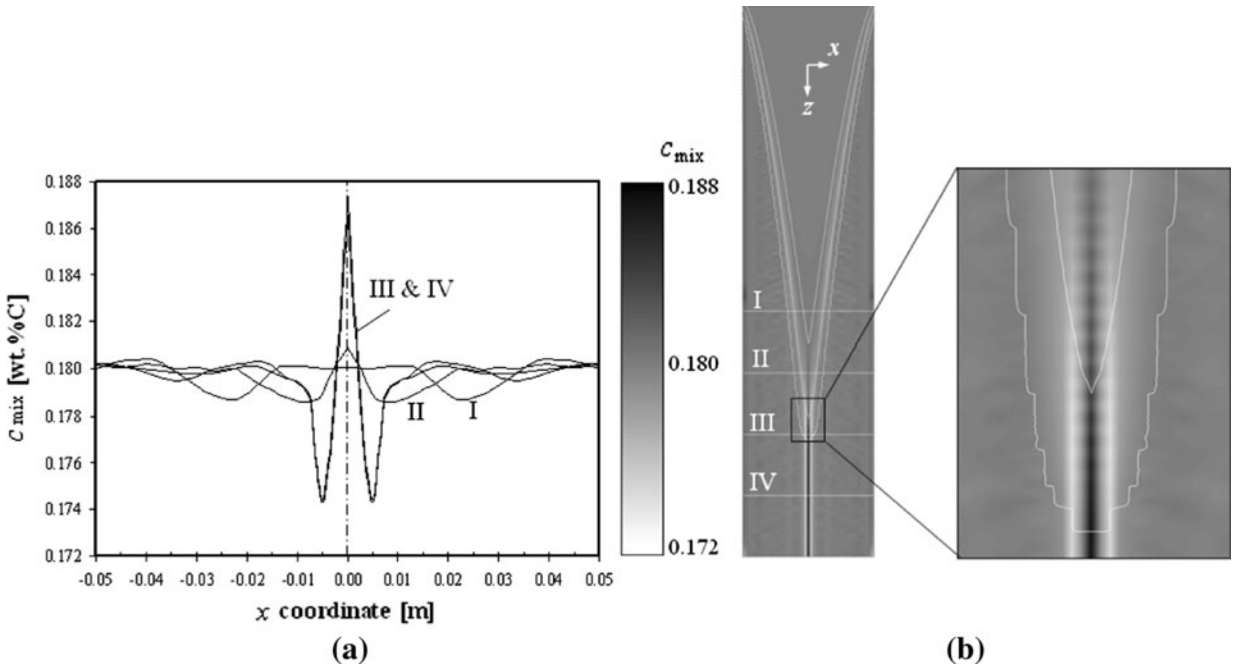

Fig. 5—Predicted macrosegregation results of Case 1. (*a*) Macrosegregation distribution profiles across the casting sections in different positions. (*b*) Macrosegregation distribution in the whole domain shown in gray scale, with light for negative segregation and dark for positive segregation. The domain is down scaled by 1:10 in *z* direction. The cross sections I, II, III, and IV are respectively 4, 5, 6, and 7 m from the coordinate origin of the calculation domain.

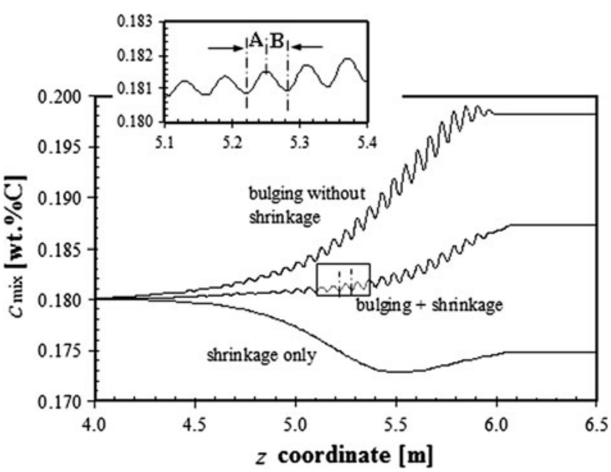

Fig. 6—Evolution of the macrosegregation along the casting centerline (Case 1), and contribution of different flow mechanisms to the centerline macrosegregation. A and B indicate two regions between a roll pair as shown in Fig. 2.

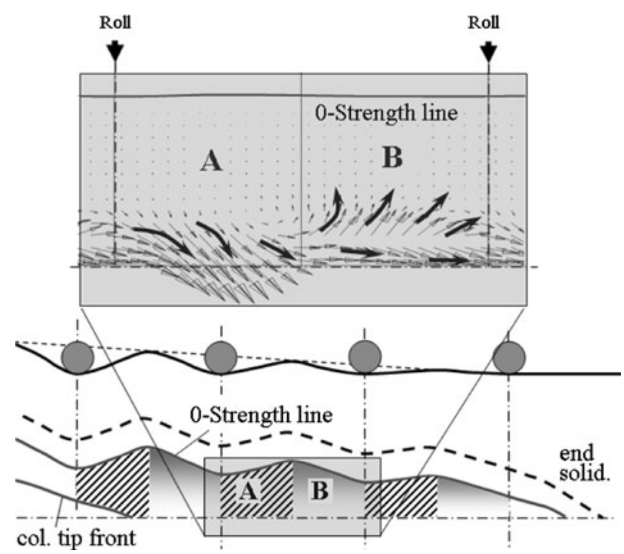

Fig. 7—Flow field of the interdendritic melt in the mushy zone of Case 1. Note that the relative velocity is plotted, and the *x*-component (vertical direction) is increased by 10 times during postprocessing. The magnitude of the relative velocity $\left|\Delta\vec{u}_{\ell-\mathrm{s}}\right|$ at the casting centerline and 4.455 m (middle of A region) distant from the coordinate origin is 9.3×10^{-4} m s^{-1}; the magnitude of the *x*-component $\left|\Delta u_{x,\ell-\mathrm{s}}\right|$ is 5×10^{-5} m s^{-1}.

To enhance the calculation efficiency, a mesh and timestep adaptation technique is used. The calculation starts with a coarse grid, and the mesh size is equal to 5 mm (total 39,600 cells). The initial timestep is set at 0.001 seconds and is adapted gradually (increased to 0.1 seconds) in the late stage when the solution is approaching steady state. In each timestep, the maximum iteration number is set to 20. Convergence criterion for enthalpy conservation equations is 10^{-7}. The convergence criteria for other conservation equations are 10^{-4} except for the continuity equation in which 0.005 was achievable in some cases. Parallel calculations are performed on an Intel Nehalem cluster using one computing node. A single node includes two quad core central processing units (CPUs) with 2.93 GHz per CPU. Each calculation for the coarse grid lasts about two to three days. Based on the steady-state solution of the coarse grid, the mesh size is adapted to 2.5 mm (total 158,400 cells). The calculation continues

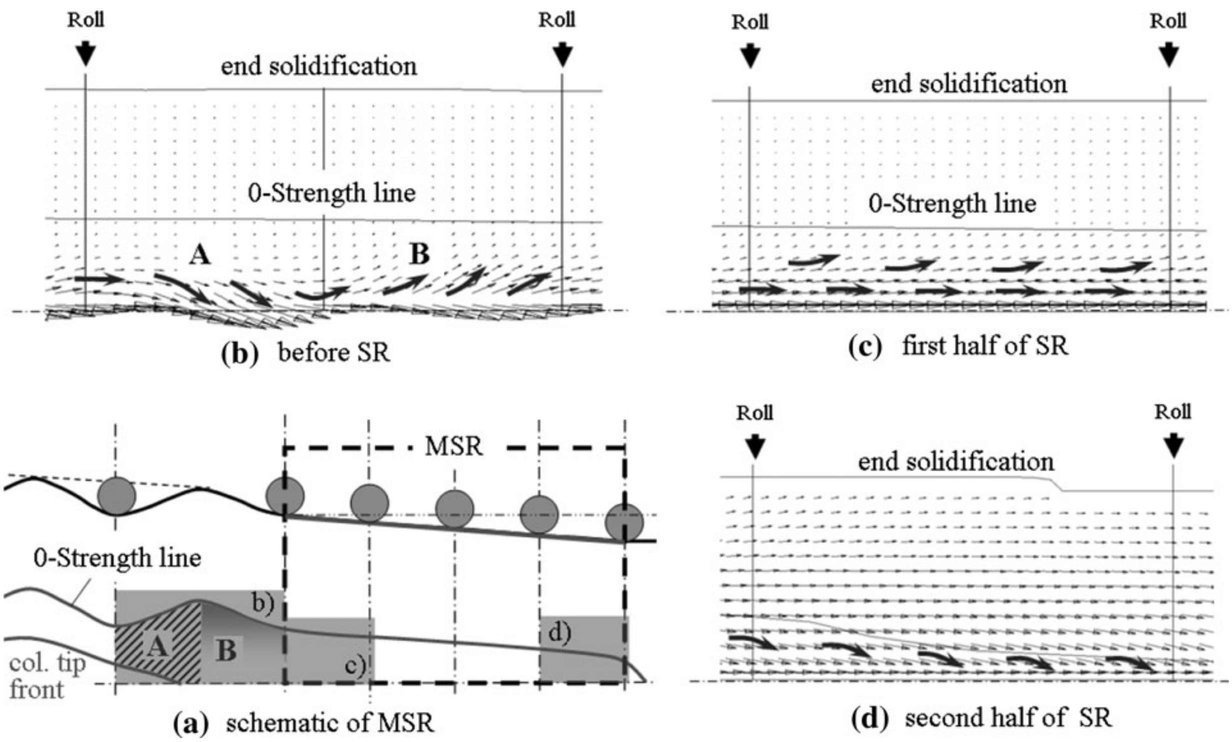

Fig. 8—Interdendritic melt flow in the mushy zone for Case 3. (*a*) Schematic of the MSR segment. (*b*) through (*d*) Relative flow fields in different regions as marked in (a). Note that the relative velocity is plotted and the *x*-component (vertical direction) is magnified by 10 during post-processing for visual clarity.

for another day with a relatively large timestep (~0.05 seconds) until the solution on the fine grid achieves steady state.

IV. CENTERLINE MACROSEGREGATION

The simulation result for Case 1, where no MSR is applied, has been published previously.[18] As a reference case, only the significant results of this case are briefly reviewed. The typical experimentally observed macrosegregation profile across the slab section is numerically predicted (Figure 5); a positive segregation peak at the casting center is accompanied by two negative segregation valleys at both sides. The evolution of the macrosegregation along the centerline (the curve of ''bulging + shrinkage'' in Figure 6) shows the accumulated effect of the series of bulging. The explanation of the formation of this kind of segregation pattern has been described by Miyazawa and Schwerdtfeger,[16] and is also supported by the current simulation with 100 bulging roll pairs (Figure 7). The positive segregation peak at the casting center is caused by the flow of enriched residual liquid toward the centerline in region A. The negative segregation valleys accompanying the centerline segregation peak are formed in region B. The explanation for this is twofold; the residual liquid flows from hot to cold regions (the hot melt entering the volume element contains the less solute than the cold liquid leaving it), and the dendritic skeleton in the mushy zone is slightly compressed. The contributions to the centerline segregation by different flow mechanisms are also investigated (Figure 6). Bulging and solidification shrinkage–induced feeding flows are the main mechanisms for the centerline segregation in the slab casting, whereas the bulging effect dominates over the feeding flow, resulting in a final positive centerline segregation.

V. PARAMETER STUDY

A. *MSR Segment Under Volume Expansion (Case 3)*

For Case 3, the MSR segment is subject to a reduction rate (ratio of the reduction amount ε to the reduction lengthl_{SR}) of 1.334×10^{-4}. The solid velocity at the entrance and exit of the MSR segment, $u_{z,s}^{IN}$, $u_{z,s}^{OUT}$, is 6.0×10^{-3} and 6.0224×10^{-3} m s^{-1}, respectively. The strand is elongated in the MSR segment. The MSR factor γ is equal to 8.52×10^{-6}, indicating that the volume of the strand in the MSR segment is expanded. The interdendritic space in the lower solid fraction region ($f_s < f_s^{0-\text{strength}}$) is enlarged, and additional melt is needed to feed the enlarged interdendritic space. The solidification shrinkage also results in feeding flow. Therefore, in the current case, both shrinkage-induced feeding flow and MSR-induced flow are imposed together to enhance the interdendritic flow in the MSR segment.

As shown in Figure 8(b), the magnitude of the calculated relative velocity $\left|\Delta\vec{u}_{\ell-s}\right|$ at the centerline and 4.455 m distant from the coordinate origin (just before the start of MSR) is 1.28×10^{-3} m s^{-1}. The melt is

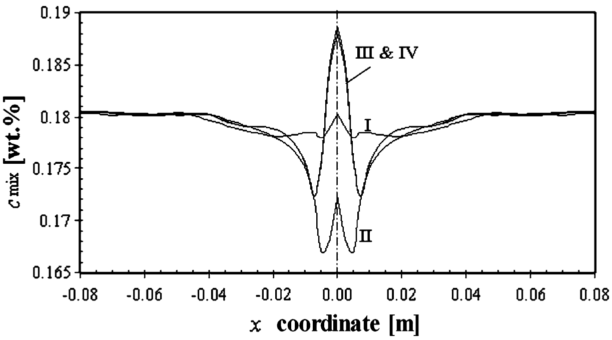

Fig. 9—Predicted macrosegregation distribution profiles across the casting sections in different positions for Case 3. The cross sections I, II, III, and IV are 4, 5, 6, and 7 m, respectively, from the coordinate origin of the calculation domain.

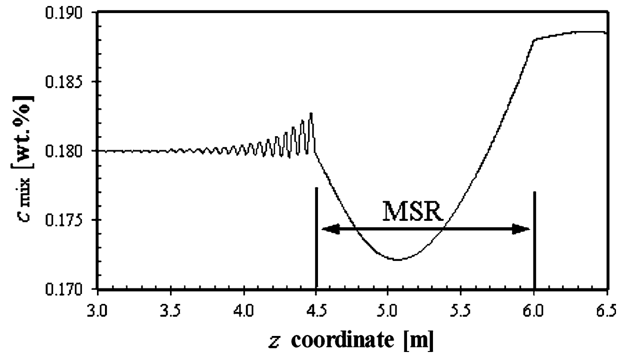

Fig. 10—Evolution of the macrosegregation along the casting centerline (Case 3).

drawn into the MSR segment. In Case 1, where no MSR is applied; the magnitude of the relative velocity $\left|\Delta\vec{u}_{\ell-\mathrm{s}}\right|$ at the same position is 9.3×10^{-4} m s^{-1}, which is significantly smaller than the velocity magnitude of Case 3. The enhanced relative velocity is because of the feeding of the enlarged interdendritic space in the MSR segment. The maximum x-component $\left|\Delta u_{x,\ell-\mathrm{s}}\right|$ at the same position for Case 3 is predicted to be 6×10^{-5} m s^{-1}, which is the same magnitude as Case 1 (5×10^{-5} m s^{-1}). In region A, the melt flows toward the casting centerline, whereas in region B, the melt flows toward the cold region. As studied previously, this kind of "pumping" flow caused by bulging is the main mechanism for the positive centerline segregation in the slab casting.[18,19]

As shown in Figure 8(c), immediately after the start of MSR, the flow is almost parallel (with a slight upward direction) to the centerline. The magnitude of the relative velocity $\left|\Delta\vec{u}_{\ell-\mathrm{s}}\right|$ at the casting centerline and 4.515 m distant from the coordinate origin (just after the start of MSR) is 1.23×10^{-3} m s^{-1}; the maximum x-component $\left|\Delta u_{x,\ell-\mathrm{s}}\right|$ is 6×10^{-6} m s^{-1}. The small upward x-component of the relative velocity together with the strong feeding flow in the casting direction would be expected to reduce c_{mix}. In the second half of the MSR segment, as shown in Figure 8(d), the flow bends toward the casting centerline. The magnitude of the relative velocity $\left|\Delta\vec{u}_{\ell-\mathrm{s}}\right|$ at the casting centerline and 5.94 m distant from the coordinate origin is 2.0×10^{-5} m s^{-1}, and the maximum x-component $\left|\Delta u_{x,\ell-\mathrm{s}}\right|$ is 5.0×10^{-6} m s^{-1}. This kind of flow pattern near the crater end enhances the positive centerline segregation.

The segregation profiles at different Sections I through IV are shown in Figure 9. At position I (4 m from the coordinate origin before the start of MSR), a typical "W"-shape of the segregation profile (*i.e.*, a positive segregation peak accompanied by two negative segregation valleys) is observed. The peak of the centerline segregation is not so high. In Section II (5 m from the coordinate origin located in the first half of the MSR segment), the "W"-shape of the segregation profile remains, but the "W" part of the c_{mix} curve moves downward. Both values of c_{mix} at the peak and valleys are smaller thanc_0; hence, no positive centerline segregation exists at this position. Positions III and IV (6 and 7 m from the coordinate origin) are located after the MSR segment. Both c_{mix} curves are overlaid with each other, but the "W" part of the c_{mix} curve moves upward. Finally, a relatively strong positive segregation peak accompanied by two strong negative segregation valleys is predicted. The deviation of c_{mix} across the slab section Δc_{mix} for Case 3 is 1.5×10^{-4}, which is greater than Case 1, for which $\Delta c_{\text{mix}}$is predicted to be 1.4×10^{-4}.

Figure 10 shows the evolution of the macrosegregation along the casting centerline. First, because of the bulging-induced "pumping" flow, positive segregation develops in a periodic pattern with respect to the z-axis. When the MSR starts, c_{mix} is significantly reduced, and even negative centerline segregation is observed. Starting from ca. 5.1 m from the coordinate origin, c_{mix} at the centerline tends to increase again. The slope of the c_{mix} curve in the second half of MSR segment is large, and a relatively large positive c_{mix} peak at the casting center is observed. After the MSR segment near the crater end, c_{mix} still increases slightly, but the slope of the curve is small.

B. *MSR Segment Under Volume Compression (Case 5)*

For Case 5, the MSR segment is subject to the same reduction rate as Case 3 (1.334×10^{-4}). The solid velocities at the entrance and exit of the MSR segment, $u_{z,\mathrm{s}}^{\mathrm{IN}}$, $u_{z,\mathrm{s}}^{\mathrm{OUT}}$, are 6.0×10^{-3} and 5.989×10^{-3} m s^{-1}, respectively. The strand in the MSR segment is shortened. The MSR factor γ is equal to -15.44×10^{-6}, indicating that the volume of the strand in the MSR segment is compressed. The interdendritic space in the lower solid fraction region ($f_{\mathrm{s}} < f_{\mathrm{s}}^{0-\mathrm{strength}}$) is reduced, and some interdendritic melt is squeezed out of the MSR segment; therefore, a backward flow is anticipated. Solidification shrinkage will induce feeding flow, which may partially compensate the backward flow.

As shown in Figure 11(b), the magnitude of $\left|\Delta\vec{u}_{\ell-\mathrm{s}}\right|$ at the centerline and 4.455 m distant from the coordinate origin (just before the start of MSR) is 6.0×10^{-4} m s^{-1}. As expected, a backward flow is predicted. The highly solute-enriched melt is squeezed out of the MSR segment. The maximum $\left|\Delta u_{x,\ell-\mathrm{s}}\right|$ at the same position

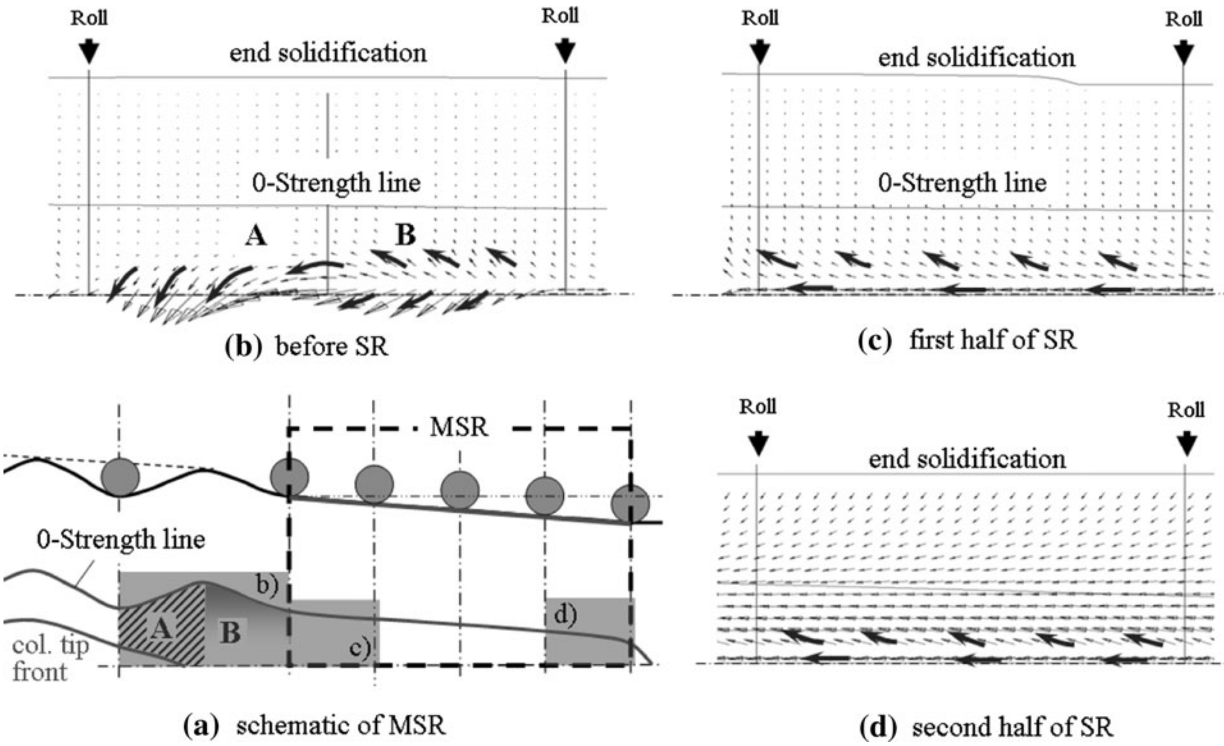

Fig. 11—Interdendritic melt flow in the mushy zone for Case 5. (*a*) Schematic of the MSR segment. (*b*) through (*d*) Relative flow fields in different regions as marked in (a). Note that the relative velocity is plotted and the *x*-component (vertical direction) is magnified by 10 during post-processing for visual clarity.

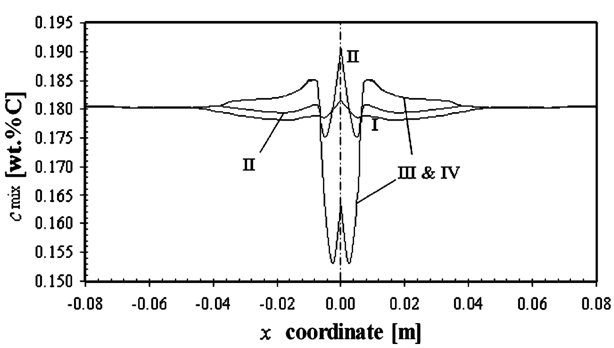

Fig. 12—Predicted macrosegregation distribution profiles across the casting sections in different positions for Case 5. The cross sections I, II, III, and IV are 4, 5, 6, and 7 m, respectively distant from the coordinate origin of the calculated domain.

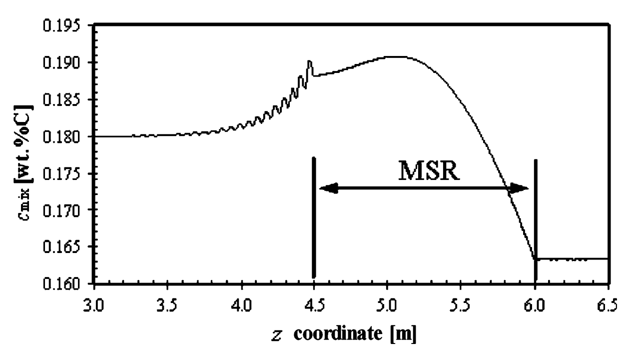

Fig. 13—Evolution of the macrosegregation along the casting centerline for Case 5.

for Case 5 is predicted to be 5.5×10^{-5} m s^{-1}, which is similar to that of Case 3 (6×10^{-5} m s^{-1}). In region A, the melt flows toward the casting centerline, whereas in region B, some melt flows toward the cold region. This kind of "pumping" flow induces a "W" shape for the segregation profile (Figure 12).

As shown in Figure 11(c), in the first half of the MSR segment, the flow is also backward and almost parallel (with a slight upward motion) to the centerline. The magnitude of $\left|\Delta\vec{u}_{\ell-\mathrm{s}}\right|$ at the casting centerline and 4.515 m distant from the coordinate origin (just after the start of MSR) is 2×10^{-4} m s^{-1}; the maximum $\left|\Delta u_{x,\ell-\mathrm{s}}\right|$ is 3×10^{-6} m s^{-1}. In the second half of MSR, as shown in Figure 11(d), the relatively large backward flow remains. The magnitude of $\left|\Delta\vec{u}_{\ell-\mathrm{s}}\right|$ at the casting centerline and 5.94 m distant from the coordinate origin is 1.1×10^{-4} m s^{-1}, and the maximum $\left|\Delta u_{x,\ell-\mathrm{s}}\right|$ is 3.0×10^{-5} m s^{-1}.

The segregation profiles at sections I to IV are shown in Figure 12. At position I (4 m from the coordinate origin before the start of MSR), the typical "W" shape of segregation profile is observed. In Section II (5 m from the coordinate origin located in the first half of MSR segment), the same shape of the segregation profile remains, but the positive peak and negative valleys become more evident. Positions III and IV (6 and 7 m

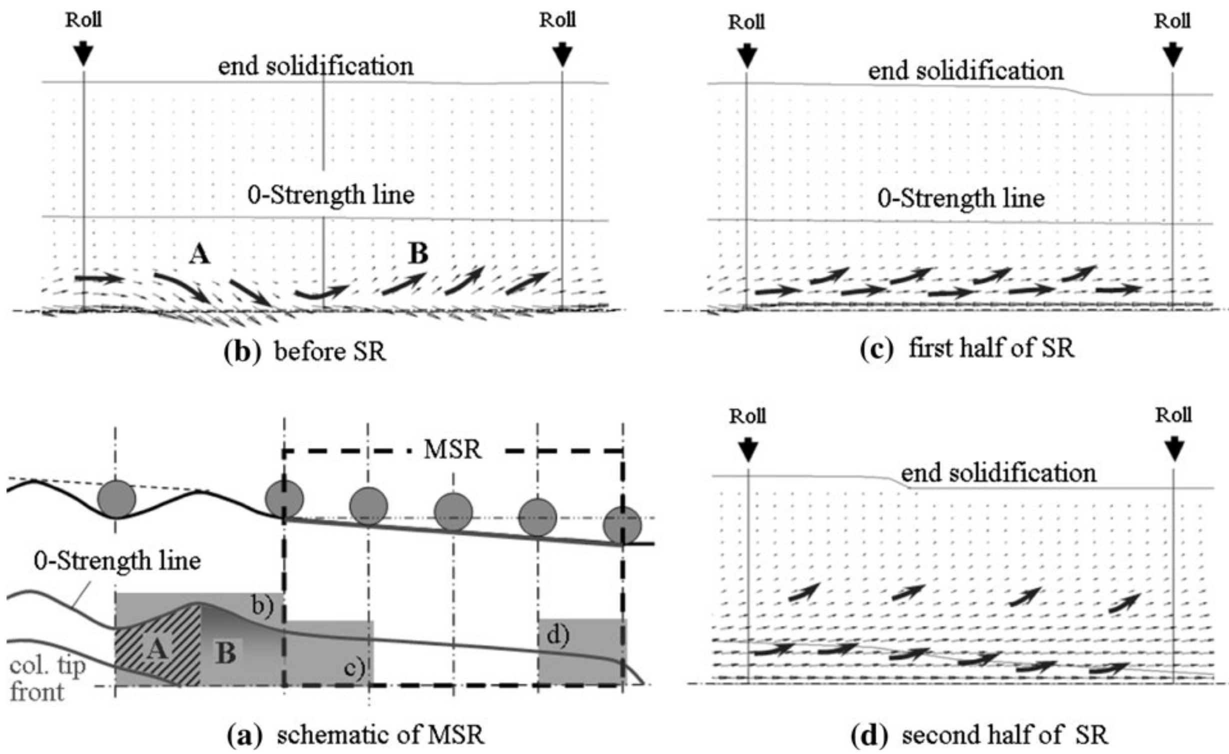

Fig. 14—Interdendritic melt flow in the mushy zone for Case 4. (*a*) Schematic of the MSR segment. (*b*) through (*d*) Relative flow fields in different regions as marked in (a). Note that the relative velocity is plotted and the x-component (vertical direction) is magnified by 10 during post-processing for visual clarity.

from the coordinate origin) are located beyond the MSR segment. Both c_{mix} peak and valleys move downward to below c_0. With the last profile, an overwhelming negative segregation in the strand core region is predicted. The deviation of c_{mix} across the slab section Δc_{mix} of Case 5 is 3.2×10^{-4}—one of the most extreme cases.

Figure 13 shows the evolution of macrosegregation along the casting centerline. First, because of the bulging-induced "pumping" flow, positive segregation develops in a periodic fashion. When the MSR starts, c_{mix} increases in the first part of the MSR segment, and the positive segregation peak reaches as high as 0.19 wt pct. In the second part of the MSR segment, c_{mix} at the centerline decreases rapidly until the end of the MSR segment.

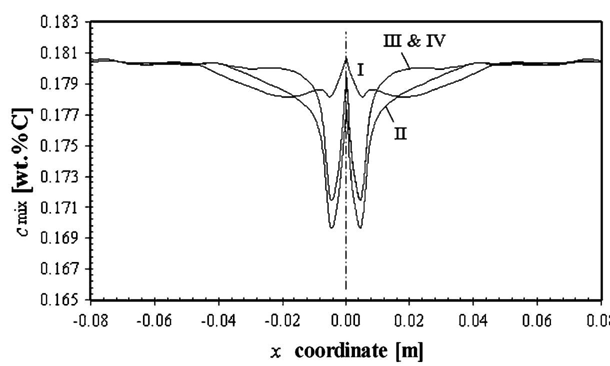

Fig. 15—Predicted macrosegregation distribution profiles across the casting sections in different positions for Case 4. The cross sections I, II, III, and IV are 4, 5, 6, and 7 m, respectively, from the coordinate origin of the calculation domains.

C. *MSR Segment Without Volume Compression or Expansion (Case 4)*

For Case 4, the reduction rate in the MSR segment is set as in previous cases at 1.334×10^{-4}. The solid velocities at the entrance and exit of the MSR segment, $u_{z,\mathrm{s}}^{\mathrm{IN}}$, $u_{z,\mathrm{s}}^{\mathrm{OUT}}$, are 6.0×10^{-3} and 6.0112×10^{-3} m s^{-1}, respectively. The strand in the MSR segment is slightly elongated. However, the MSR factor γ is equal to 0, indicating that no volume compression or expansion is applied in the MSR segment. The interdendritic space in the lower solid fraction region ($f_{\mathrm{s}} < f_{\mathrm{s}}^{0\text{-strength}}$) is not influenced by MSR. Therefore, the main mechanism for the interdendritic flow in the MSR segment is a result of solidification shrinkage.

As shown in Figure 14(b), the magnitude of $\left|\Delta\vec{u}_{\ell-\mathrm{s}}\right|$ at the centerline and 4.455 m from the coordinate origin (just before the start of MSR) is 8.3×10^{-4} m s^{-1}. This is the same magnitude as Case 1 (9.3×10^{-4} m s^{-1}) in which no MSR is applied. The melt is drawn into the MSR segment by the solidification shrinkage. The maximum $\left|\Delta u_{x,\ell-\mathrm{s}}\right|$ at the same position for Case 4 is predicted to be 6×10^{-5} m s^{-1}, which is the same magnitude as Case 1 (5×10^{-5} m s^{-1}). A "pumping" flow pattern similar to that of Case 1, responsible for the formation of the positive centerline segregation, is predicted for the current case.

As shown in Figure 14(c), in the first half of the MSR segment, the flow pattern is similar to Case 3 (*i.e.*, parallel, with a slight upward motion, to the centerline), but it is much smaller. The magnitude of $\left|\Delta\vec{u}_{\ell-s}\right|$ at the casting centerline and 4.515 m from the coordinate origin is 7.2×10^{-4} m s^{-1}, in comparison with Case 3, where the magnitude of $\left|\Delta\vec{u}_{\ell-s}\right|$ at the same position is 1.23×10^{-3} m s^{-1}. The maximum $\left|\Delta u_{x,\ell-s}\right|$ is 5×10^{-6} m s^{-1}, which is the same magnitude as Case 3 (6×10^{-6} m s^{-1}). The small upward x-component of the relative velocity together with the feeding flow in this region would reduce c_{mix}. In the second half of the MSR segment, as shown in Figure 14(d), the interdendritic melt flows toward the cold region. The magnitude of $\left|\Delta\vec{u}_{\ell-s}\right|$ at the casting centerline and 5.94 m from the coordinate origin is 9.0×10^{-5} m s^{-1}, and the maximum $\left|\Delta u_{x,\ell-s}\right|$ is 1.0×10^{-6} m s^{-1}. This kind of flow pattern near the crater end tends to increase the centerline c_{mix} peak again.

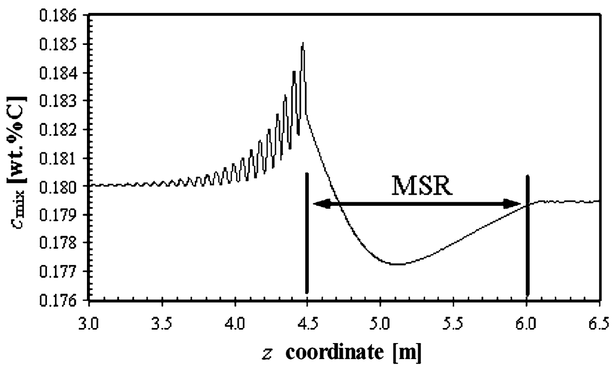

Fig. 16—Evolution of the macrosegregation along the casting centerline (Case 4).

The segregation profiles at Sections I through IV are shown in Figure 15. At position I (4 m from the coordinate origin), before the start of MSR, a typical "W" shape of segregation profile is observed. In Section II (5 m from the coordinate origin), located in the first half of MSR segment, the "W" shape of the segregation profile remains, but the "W" part of the c_{mix} curve moves downward. Both the peak and the valleys of c_{mix} are smaller than c_0; hence, no positive centerline segregation is found at this position. The c_{mix} variation tendency from positions I through II is also similar to Case 3, but the enhanced negative segregation valley is not as strong as in Case 3. Positions III and IV (6 and 7 m from the coordinate origin) are located after the MSR segment. The c_{mix} curves are overlaid, but the "W" part of the

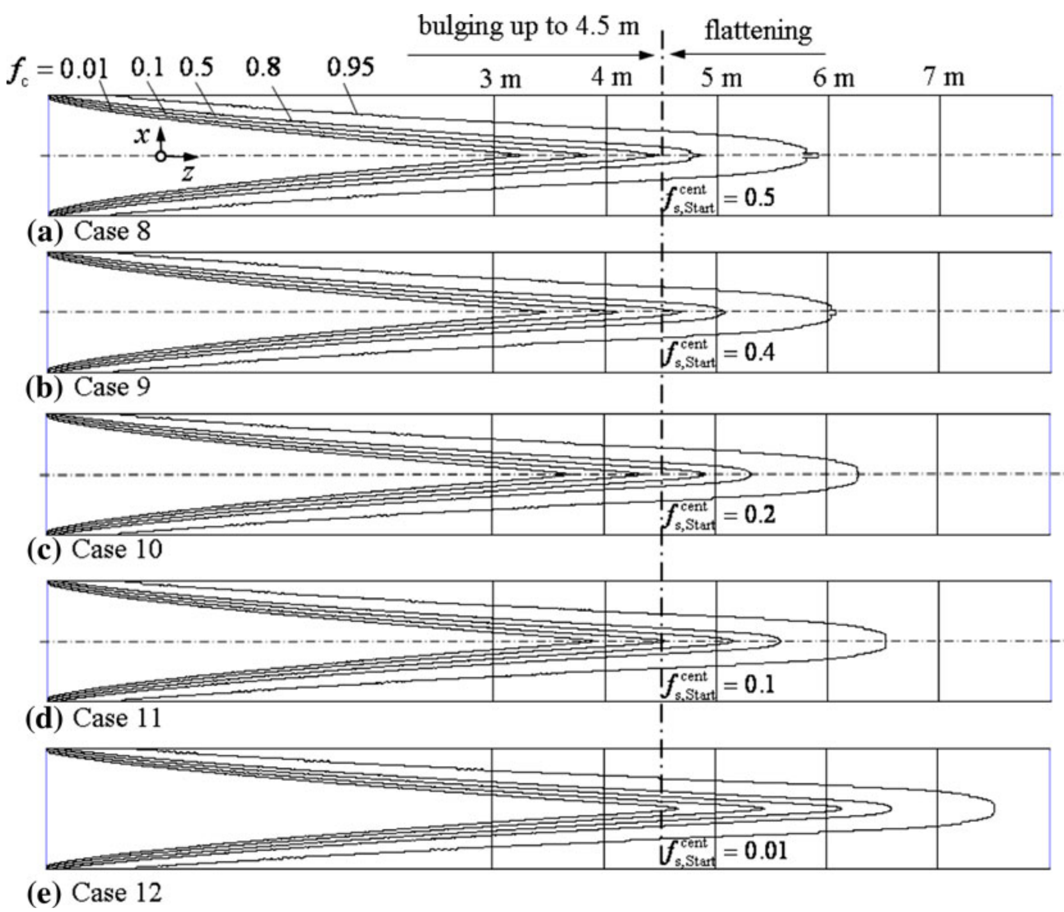

Fig. 17—Overview of the calculated crater end positions by using a so-called modified heat capacity method.[25] (*a*) Case 8: flattening starts at $f_{\text{s,Start}}^{\text{cent}} = 0.5$, and the simulation is made with 65 pct of Δh_{f} being considered; (*b*) Case 9: flattening at $f_{\text{s,Start}}^{\text{cent}} = 0.4$, with 70 pct of$\Delta h_{\text{f}}$; (*c*) Case 10: flattening at $f_{\text{s,Start}}^{\text{cent}} = 0.2$, with 75 pct of$\Delta h_{\text{f}}$; (*d*) Case 11: flattening at $f_{\text{s,Start}}^{\text{cent}} = 0.1$, with 80 pct of$\Delta h_{\text{f}}$; (*e*) Case 12: flattening at $f_{\text{s,Start}}^{\text{cent}} = 0.01$, with 100 pct of Δh_{f}.

curves moves upward again. Coincidently, the peak value of the "W" curve of $c_{\rm mix}$ is equal to the nominal composition of the alloy c_0. The $c_{\rm mix}$ value at the two valleys is 17.2×10^{-4}. A relatively large negative segregation near the casting centerline is predicted.

Figure 16 shows the evolution of the macrosegregation along the casting centerline. First, because of the bulging-induced "pumping" flow, positive segregation shows a periodic pattern. In the first half of the MSR segment, $c_{\rm mix}$ is significantly reduced, and even negative centerline segregation is obtained. Starting from ca. 5.1 m from the coordinate origin, $c_{\rm mix}$ at the centerline tends to increase again. At the end of MSR, $c_{\rm mix}$ reaches almost c_0.

D. *Flattening (Cases 8 Through 12)*

Previous investigations[16–19] have shown that positive centerline segregation in the slab casting is predominately caused by bulging. Therefore, the following simple antibulging idea is proposed: "flattening" the slab surface during the late stage of solidification. Flattening can be considered a special case of MSR in which the reduction amount ε is set to zero and $u_{z,\rm s}^{\rm IN} = u_{z,\rm s}^{\rm OUT}$.

Five simulations were performed in Cases 8 through 12 (Figure 17). The real position of the starting point of flattening is actually set at the same position, namely 4.5 m from the coordinate origin. A so-called modified heat capacity method[25] is used to adjust the crater end position. In each simulation case, only a portion of latent heat caused by solidification $\Delta h_{\rm f}$ is accounted for. This treatment facilitates the numerical parameter study of varying the crater end position while keeping the casting boundary conditions unchanged. For example, in Case 8 when 65 pct of the solidification latent heat $\Delta h_{\rm f}$ is accounted for, the $f_{\rm s}$ = 0.5 isoline ends at the starting point of flattening. In Case 12 when 100 pct of $\Delta h_{\rm f}$ is accounted for, the $f_{\rm s}$ = 0.01 isoline ends at the starting point of flattening.

Simulation results are summarized in Figures 18 and 19 and in Table III. In Case 8, where flattening starts at $f_{\rm s,Start}^{\rm cent}$ = 0.5, the peak $c_{\rm mix}$ at the slab center reaches as high as = 18.7×10^{-4}, whereas the minimum $c_{\rm mix}$ at the valleys is only 16.7×10^{-4}. The segregation deviation $\Delta c_{\rm mix}$ is high at 2.2×10^{-4}. When flattening starts at a position of $f_{\rm s,Start}^{\rm cent}$, less than 0.4, the predicted $\Delta c_{\rm mix} \leq 0.8 \times 10^{-4}$. This study indicates that a delayed flattening will degrade the flattening efficiency. Before flattening starts, because of the bulging-induced "pumping" flow, a periodic positive centerline segregation develops along the z-axis (Figure 19). The solid volume fraction at the casting center is less than 0.4; thus, the centerline positive segregation is not severe. If the bulging is suppressed by a subsequent "treatment" of flattening, the core region of the slab will solidify continuously with feeding as the only mechanism for the interdendritic flow. Feeding flow tends to reduce centerline$c_{\rm mix}$. Therefore, the positive segregation because of bulging can be compensated to some extent by flattening. When flattening is imposed too early ($f_{\rm s,Start}^{\rm cent} \leq 0.1$), for example, Cases 11 and 12, a relatively large negative segregation zone near the casting center (Figure 18) is predicted, although the concentration deviation $\Delta c_{\rm mix}$ is small (0.6).

When comparing flattening (Cases 8 through 12) and MSR (Cases 2 through 7), flattening seems to produce less segregation. By varying the MSR parameters, the segregation problem could be improved. It can be concluded that it is easier to control the flattening process parameters than to control the MSR process parameters, as a relatively large $f_{\rm s,Start}^{\rm cent}$ variation window (from 0.2 to 0.4) for flattening would produce satisfactory results. In the MSR cases, the final segregation is sensitive to the MSR parameters.

VI. DISCUSSION

A. *Principle of MSR*

When steady-state columnar solidification in the slab casting is reached, the centerline segregation caused by

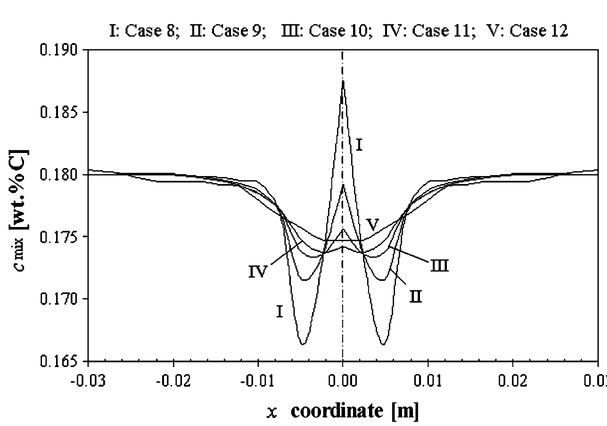

Fig. 18—Final macrosegregation profiles at the outlet section of the slab. Flattening is imposed at different positions, corresponding to Cases 8 through 12 (Fig. 17).

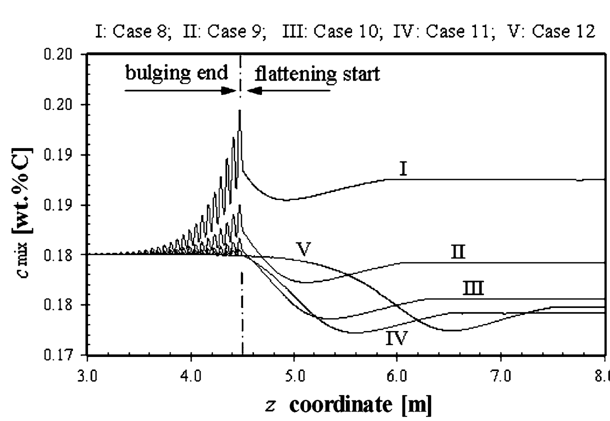

Fig. 19—Macrosegregation evolution along the casting centerline. Flattening is assumed to start at a different centerline solid fraction, corresponding to Cases 8 through 12 (Fig. 17).

deformation of the mushy zone can be analyzed by the following equation:

$$\vec{u}_s \cdot \nabla c_{mix} = -f_\ell \Delta \vec{u}_{\ell-s} \cdot \nabla c_\ell + f_s(c_\ell - c_s)\nabla \cdot \vec{u}_s \qquad [26]$$

This equation is derived (Appendix) from the mass and species conservations with an additional simplifying assumption that the liquid and solid have equal and constant density ($\rho_\ell = \rho_s$ = constant). The error caused by this assumption can be quantified by the residual between the left-hand side (LHS) and the sum of the right-hand side (RHS) of Eq. [26], analyzed in Figures 20(d) and 21(d). This residual is relatively small because the contribution of shrinkage-induced flow to the centerline segregation becomes small in the presence of bulging- and MSR-induced flow.

The LHS of Eq. [26], $\vec{u}_s \cdot \nabla c_{mix}$, corresponds to the time derivative of c_{mix} and dc_{mix}/dt, in the Lagrangian frame referring to the moving solid phase. A time integral of the LHS over all volume elements along the slab centerline $\left(c_0 + \sum\left(\vec{u}_s \cdot \nabla c_{mix} \cdot \delta t\right)\right)$ gives the c_{mix} profile along the centerline, where δt is the timestep required for the solid dendrites passing through one volume element. Examples of the time integral of the LHS (Cases 3 and 5) are shown in Figures 20(a) and 21(a). The dashed lines in those figures are the time integral of the LHS of Eq. [26], and are identical to the $c_{mix} - z$ profiles as simulated by the numerical model (Figures 10 and 13).

The formation of the centerline segregation caused by the deforming mushy zone can be analyzed according to the contributions of two parts, namely the first RHS term $(-f_\ell \Delta \vec{u}_{\ell-s} \cdot \nabla c_\ell)$ and the second RHS term $(f_s(c_\ell - c_s)\nabla \cdot \vec{u}_s)$ of Eq. [26]. The first RHS term calculates the macrosegregation caused by the MSR-induced flow of the interdendritic melt ($\Delta \vec{u}_{\ell-s}$), in which a concentration gradient (∇c_ℓ) exists. Flow in the direction of ∇c_ℓ, corresponding to highly segregated melt being replaced by the less segregated melt, leads to a reduction of c_{mix}. The second RHS term calculates the macrosegregation caused by the non-divergence-free deforming mushy zone, $\nabla \cdot \vec{u}_s \neq 0$. For the solidification of plain carbon steel, the liquid concentration of carbon (c_ℓ) is always larger than that of solid(c_s). Therefore, a positive $\nabla \cdot \vec{u}_s$ tends to increase c_{mix}, which coincides with the case when the volume of the strand in the MSR segment is in expansion ($\gamma > 0$) and the solute-enriched melt is drawn into the enlarged interdendritic space in the MSR segment. A negative $\nabla \cdot \vec{u}_s$ tends to decrease c_{mix}, corresponding to MSR segment compression ($\gamma < 0$) in which the solute-enriched interdendritic melt is squeezed out of the segment.

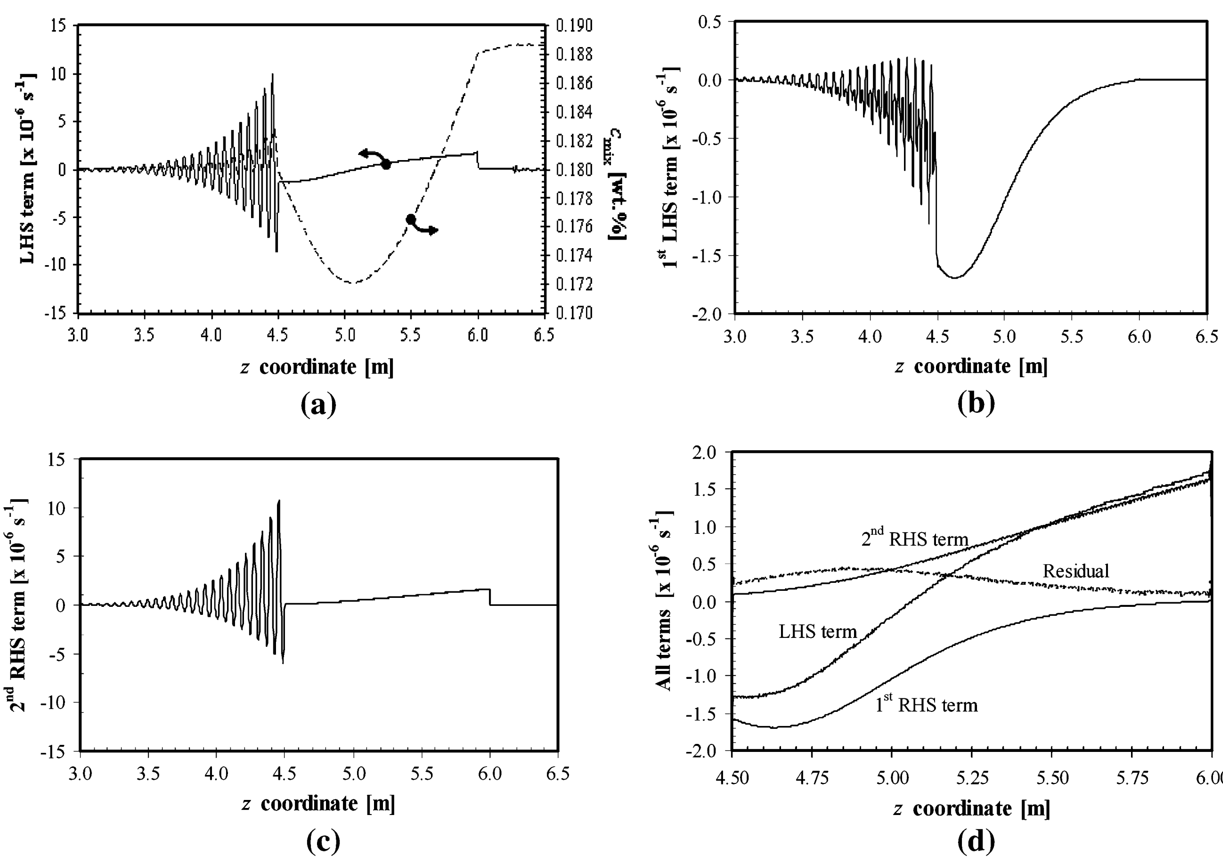

Fig. 20—Macrosegregation caused by the volume expansion because of MSR (Case 3). (*a*) Plot of LHS term of Eq. [26] in solid line, shown together with the time integral of the LHS term $\left(c_0 + \sum\left(\vec{u}_s \cdot \nabla c_{mix} \cdot \delta t\right)\right)$ in the dashed line, which is identical to the $c_{mix} - z$ profile of the numerical result in Fig. 10; (*b*) Plot of the first RHS term of Eq. [26]; (*c*) Plot of the second RHS term of Eq. [26]; (*d*) In the MSR segment, the contributions of all terms of Eq. [26] are compared (solid lines), and the residual between the LHS term and the sum of RHS terms is also shown (dashed line).

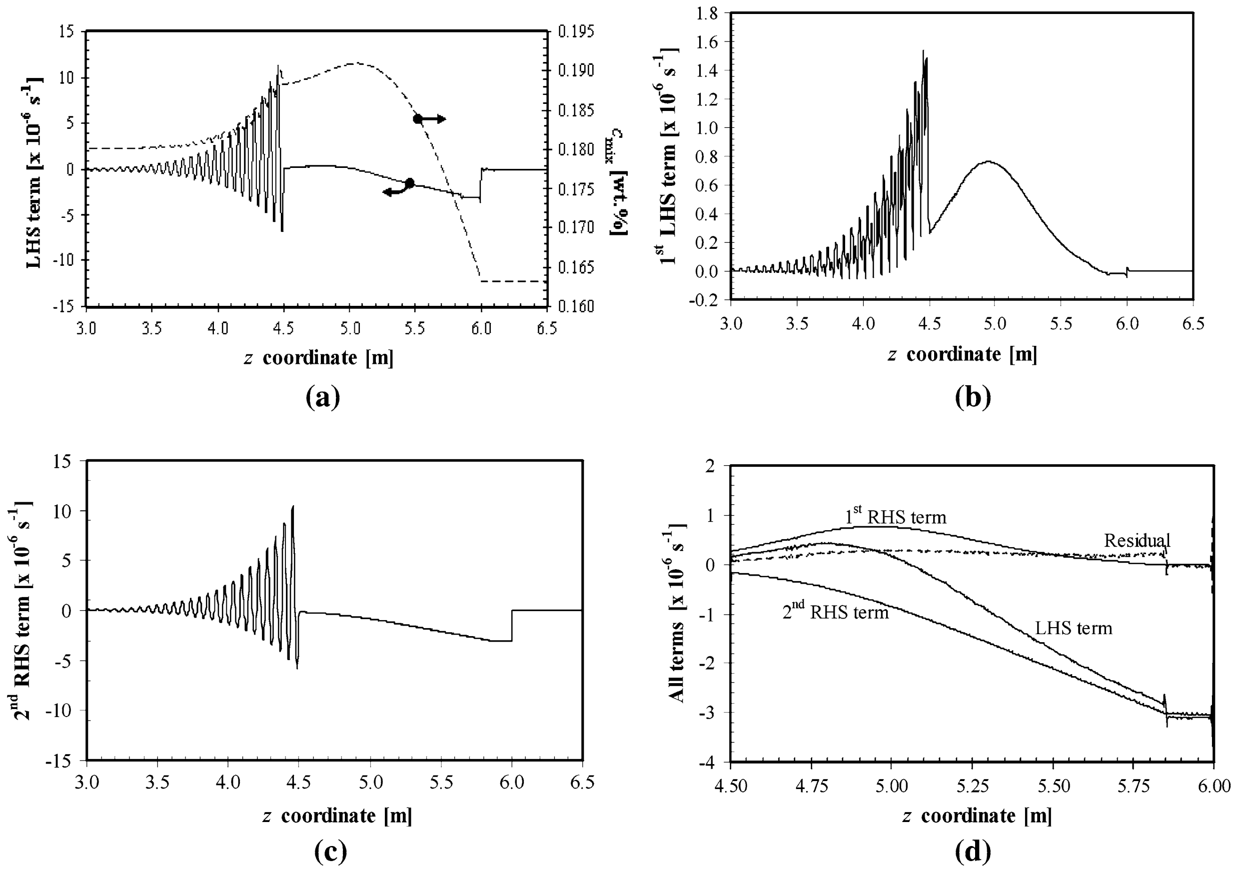

Fig. 21—Macrosegregation caused by the volume expansion because of MSR (Case 5). (*a*) The LHS term of Eq. [26] is shown with a solid line, together with the time integral of the LHS term $\left(c_0 + \sum\left(\vec{u}_s \cdot \nabla c_{mix} \cdot \delta t\right)\right)$ shown with a dashed line, which is identical to the $c_{mix} - z$ profile of the numerical result of Fig. 13; (*b*) Plot of the first RHS term of Eq. [26]; (*c*) Plot of the second RHS term of Eq. [26]; (*d*) In the MSR segment, the contributions of each term in Eq. [26] are compared (solid lines), and the residual between the LHS term and the sum of RHS terms is also shown (dashed line).

As detailed in Figure 20, all three terms of Eq. [26] for Case 3 are calculated and compared. In this case, the volume of the strand in the MSR segment is expanded, $\gamma > 0$ and $\nabla \cdot \vec{u}_s > 0$. The contribution of the second RHS term of Eq. [26] is always positive in the MSR segment, hence increasing the centerlinec_{mix}, as shown in Figures 20(c) and (d). The contribution of the first RHS term of Eq. [26] is negative, as the flow is mostly in the same direction as the concentration gradient (Figure 8), hence reducing c_{mix}, as shown in Figures 20(b) and (d). The contribution of the first RHS term seems to dominate in the first half of the MSR segment (up to ca. 5.1 m from the coordinate origin), whereas in the second half of the MSR segment, the role of the second RHS term is dominant. In total, the contribution of the second RHS term is much larger than the first RHS term, and a positive centerline segregation occurs in the MSR segment. The calculated contributions of the LHS and RHS terms before MSR segment, where bulging occurs, are also plotted in Figures 20 (a) through (c). Although the magnitude of the bulging, as calculated by Eq. [25], is reduced to only 0.2 mm just before the MSR segment starts, the effects of the bulging on both the first and second RHS terms of Eq. [26], between each bulging roll pair, are strong. A consequence of the bulging is the relatively strong evolution of the periodic c_{mix} profile. Details about bulging are not discussed here.

As shown in Figure 21, all three terms of Eq. [26] for Case 5 are calculated and compared. In this case, the MSR segment is compressed, $\gamma < 0$ and $\nabla \cdot \vec{u}_s < 0$. The contribution of the second RHS term of Eq. [26] is always negative in the MSR segment, hence reducing the centerline c_{mix}, as shown in Figures 21(c) and (d). The contribution of the first RHS term of Eq. [26] is positive, as the flow is mostly in the opposite direction of the concentration gradient (Figure 11), hence increasing c_{mix}, as shown in Figures 21(b) and (d). The contribution of the first RHS term seems to show a stronger effect in the first half of the MSR segment (up to ca. 5.1 m from the coordinate origin), whereas the role of the second RHS term is dominant in the second half of the MSR segment. Overall, the contribution of the second RHS term is much larger than the first RHS term, and negative centerline segregation occurs in the MSR segment.

Summarizing the previous discussions, the centerline segregation of the slab casting is influenced by MSR through the following mechanisms: the MSR-induced interdendritic flow and the non-divergence-free deformation

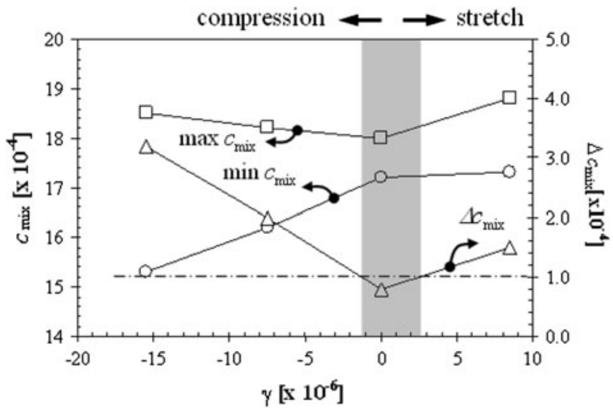

Fig. 22—The calculated $\Delta c_{mix} - \gamma$ map based on the benchmark of reduced geometry. Here the starting position of MSR is kept at $f^{cent}_{s,Start} = 0.4$.

of the dendritic skeleton in the mushy zone. These mechanisms can be quantitatively analyzed through the two RHS terms of Eq. [26]. According to the current parameter study, the contribution of the second RHS term generally dominates the first RHS term; therefore, the role of MSR can be primarily analyzed with the second RHS term of Eq. [26]. A volume compression of the strand in the MSR segment tends to decrease c_{mix}; a volume expansion of the strand in the MSR segment tends to increase c_{mix}, whether the MSR segment is in expansion or compression is determined by γ. A general expectation is that compression of the MSR segment with $\gamma < 0$ would compensate the positive centerline segregation originating from the bulging ahead of the MSR segment.

It is often assumed that, when a certain amount of reduction (ε) is applied, the MSR will be under compression to reduce the centerline positive segregation. According to Eq. [18] and the current simulation results, this is not always true. The value of γ is the outcome of ε, l_{SR}, $u^{IN}_{z,s}$, and $u^{OUT}_{z,s}$. Whether the MSR segment is under compression or expansion depends not only on the reduction amount (ε) in the thickness but also on the deformation behavior in the longitudinal (casting) direction ($u^{IN}_{z,s}$, $u^{OUT}_{z,s}$). By keeping the rest of the MSR parameters constant, γ can be varied with $u^{OUT}_{z,s}$. Thus, one may deduce that the deformation in the slab width direction may influence the result as well. The current model has neglected the deformation in the slab width dimension. Some studies have shown that the lateral deformation in the width direction does have significant influence on MSR efficiency for the bloom casting within a certain range of width-to-thickness ratio,[27,28] but the influence becomes small with an increasing width-to-thickness ratio of casting.

B. *Parameters Influencing MSR Efficiency*

The MSR efficiency is evaluated based on the deviation of c_{mix} in the cross section of the solidified slab Δc_{mix}. In principle, the MSR efficiency depends strongly on γ. Therefore, Δc_{mix} together with the minimum and maximum c_{mix} across the casting section are plotted as function of γ in Figure 22. We find that the best MSR efficiency can be achieved when γ is about 0. This conclusion does not contradict the previous expectation that a slight compression of the MSR segment ($\gamma < 0$) would produce optimal results. We know that, in the case of $\gamma = 0$, the contribution of the second RHS term disappears. In this special case, only the contribution of the first RHS term remains. As the flow pattern is significantly modified by flattening the slab surface in the MSR segment, the centerline segregation is modified through the contribution of the first RHS term. Therefore, according to the current benchmark, if a Δc_{mix} of 1.0×10^{-4} is defined as the tolerance limit, the MSR factor γ should be controlled in the gray band (Figure 22) between -1.2 and 2.8×10^{-6}.

Please note that the divergence-free ($\gamma = 0$) scenario occurs when $u^{IN}_{z,s} = 0.006$ m/s and $u^{OUT}_{z,s} = 0.005989$ m/s, rather than $u^{IN}_{z,s} = u^{OUT}_{z,s}$. With $u^{IN}_{z,s} = u^{OUT}_{z,s}$, corresponding to Case 2 (Table III), γ is equal to -7.44×10^{-6}, and the MSR efficiency is not optimal.

To investigate the influence of the MSR position, two simulations by varying the start point of MSR ($f^{cent}_{s,Start} = 0.2$) were performed, as shown in Table III. It was shown that an early start of MSR ($f^{cent}_{s,Start} = 0.2$) produces a better MSR efficiency than a later start of MSR ($f^{cent}_{s,Start} = 0.4$). Note that the current model did not consider the probable bulging during the MSR segment. If the MSR starts and ends too early, where the solidified shell in the MSR is not sufficiently strong, bulging may occur in the MSR segment as well, and this will, to some extent, degrade the MSR efficiency.

Another interesting phenomenon observed in the current work is that flattening seems to result in less centerline segregation than MSR. This phenomenon does not actually contradict the previous studies. As the positive centerline segregation in slab casting originates mainly from bulging, this segregation can be logically reduced with an idea of countering bulging phenomena. Flattening is sufficient to achieve this goal. An advantage of flattening is that a relatively large $f^{cent}_{s,Start}$ variation range (from 0.2 to 0.4) can produce satisfactory results. One would argue that it is difficult or unrealistic to implement the flattening process in industry. The aforementioned numerical study, however, implies that keeping a flat surface (avoiding bulging) is even more important than controlling other MSR parameters.

Additionally, the current parameter studies were carried out on a reduced slab benchmark. Because of the high calculation cost (each simulation lasts ca. four days), the number of case simulations and the scale of the geometry were limited. However, the $\Delta c_{mix} - \gamma$ map (Figure 22) provides an example and guideline for future work. Calculations with an industrial casting geometry, more realistic boundary conditions, and varying combinations of the MSR (ε, l_{SR}, $u^{IN}_{z,s}$, and $u^{OUT}_{z,s}$) and bulging (δ^b_{max}, N, and l_b) parameters would provide valuable information to optimize the real production process.

C. *Model Uncertainties and Additional Improvements*

A thermomechanical model has not been implemented, and the impact of this on the model cannot be ignored. The solid velocity $\vec{u}_s$ has been estimated according to Miyazawa and Schwerdtfeger,[16] with a suitable modification. An exponential curve is used to describe $u^b_{x,s}$ for the low solid fraction zone (Eq. [17]) instead of using a linear reduction of $u^b_{x,s}$ (Eq. [16]).[16,17] The current authors support the hypothesis that most deformation in the mushy zone occurs near the strand core, where the solid volume fraction is the lowest rather than a homogeneous deformation across the whole section of the mushy zone. This opinion has been supported by many experimental studies[29–31]; however difficulties in determining the empirical constants in Eq. [17] remain. Another issue is the volume change of the solid-state phase transition (from δ ferrite to γ austenite), which may play an important role in the mechanical deformation as well. For future development, incorporating the thermomechanical model in the multiphase solidification model as suggested by Bellet or Fachinotti[32,33] is desirable. Otherwise, the one-way coupling as suggested by Kajitani *et al.*[17] is also an intermediate solution.

Industry practice has shown that porosity usually accompanies centerline segregation. Explicit modeling of the pore formation by including a gas phase would dramatically increase the complexity of the model and the calculation cost. An argument in favor of ignoring the pore formation in our numerical model is that one of the MSR target is to suppress the pore formation. Actually, no pores are expected after an adequate MSR.

Other uncertainties related to deformation in the width direction may not be so severe for the slab casting when the width-to-thickness ratio is sufficiently large.[27,28] For the slab/bloom casting with small width-to-thickness ratio, 3D calculation is desired. Crack formation is out of the scope of this study; however, it is an additional limiting factor in the MSR process, as shown in Figure 1,[2,3] which should be noted when the model is applied to any real continuous process optimization.

VII. CONCLUSIONS

A two-phase columnar solidification model has been used to study MSR to reduce the centerline segregation in slab casting. A benchmark slab casting (9-m long, 0.215-m thick) of plain carbon steel was simulated. By studying the MSR process parameters, such as the position of MSR, the reduction rate, the deformation behavior of the strand in the MSR segment in the longitudinal direction, and flattening of the slab surface, new knowledge and insight into the MSR process has been learned and discussed. The following conclusions were made after completing this study:

1. From an engineering perspective, the purpose of MSR is to minimize the centerline segregation, which results from bulging- and solidification shrinkage–induced feeding flow through a "designed" mechanical deformation. The contribution of feeding flow is relatively small in the presence of bulging- and MSR-induced flow.
2. Two mechanisms of the MSR process modify the centerline segregation. The first one is to establish a favorable interdendritic flow, which can modify the centerline c_{mix} as the interdendritic melt of one concentration is replaced with melt from neighboring regions of different concentration. The second mechanism is caused by the non-divergence-free deformation of dendritic skeleton in the mushy zone. The deforming mushy zone draws or squeezes the solute-enriched melt in or out of the MSR segment, modifying the local c_{mix}. The contribution of the second mechanism dominates the first one. A compressed MSR segment tends to reduce the centerline c_{mix}, whereas a MSR segment in expansion tends to increase the centerline c_{mix}.
3. A $\Delta c_{mix}-\gamma$ map is established to empirically evaluate the MSR efficiency. The MSR factor (γ), evaluating the volume-averaged divergence of the solid velocity in the MSR segment, is defined by Eq. [18] based on ε, l_{SR}, $u^{IN}_{z,s}$, and $u^{OUT}_{z,s}$. In this sense, the MSR efficiency depends not only on the reduction amount in the slab thickness but also on the deformation in the longitudinal direction (elongation or shortening).
4. A numerical study on flattening, namely an antibulging process that flattens the slab surface between roll pairs, is carried out. Implementing the flattening process in industry might be difficult to realize, but the modeling results imply that maintaining a flat surface is more important than controlling other MSR parameters.
5. The modeling results have shown that an early start of MSR or flattening leads to better MSR or flattening efficiency than a late start.
6. The current model has been verified to have great application potential for the qualitative study of the MSR efficiency and its influencing parameters. However, attention should be paid to when it is applied for quantitative calculation of real continuous casting process. Uncertainties in the model include (1) the estimated solid velocity, (2) neglected porosity and crack formation, (3) neglected deformation of the slab in width direction, and (4) neglected possible bulging in the MSR segment. For this, additional model refinements are still needed.

ACKNOWLEDGMENTS

The financial support by the Austrian Federal Ministry of Economy, Family and Youth, the National Foundation for Research, Technology and Development, voestalpine Stahl, Siemens VAI Metal Technologies and voestalpine Stahl Donawitz is gratefully acknowledged.

APPENDIX: DERIVATION OF EQ. [26]

With the following assumptions:

- Steady state is achieved (*i.e.*, $\partial()/\partial t = 0$)
- Liquid and solid have an equal and constant density

($i.e.$, $\rho_\ell = \rho_s$ = constant)

From the mass conservation equation Eq. [1], with $f_\ell + f_s = 1$, the following is true:

$$\nabla \cdot \left(f_\ell \vec{u}_\ell\right) = \vec{u}_s \cdot \nabla f_\ell - f_s \nabla \cdot \vec{u}_s \quad \text{[A1]}$$

From the species conservation equation Eq. [3], the following is true:

$$c_\ell \nabla \cdot \left(f_\ell \vec{u}_\ell\right) + f_\ell \vec{u}_\ell \cdot \nabla c_\ell + \vec{u}_s \cdot \nabla (f_s c_s) + f_s c_s \nabla \cdot \vec{u}_s = 0 \quad \text{[A2]}$$

Substituting $\nabla \cdot \left(f_\ell \vec{u}_\ell\right)$ with $\vec{u}_s \cdot \nabla f_\ell - f_s \nabla \cdot \vec{u}_s$ in Eq. [A2], the following is true:

$$\vec{u}_s \cdot \nabla (f_\ell c_\ell + f_s c_s) - f_\ell \vec{u}_s \cdot \nabla c_\ell + f_\ell \vec{u}_\ell \cdot \nabla c_\ell = f_s (c_\ell - c_s) \nabla \cdot \vec{u}_s \quad \text{[A3]}$$

where $f_\ell c_\ell + f_s c_s = c_{\text{mix}}$, so Eq. [26] is obtained as follows:

$$\vec{u}_s \cdot \nabla c_{\text{mix}} = -f_\ell \Delta \vec{u}_{\ell-s} \cdot \nabla c_\ell + f_s (c_\ell - c_s) \nabla \cdot \vec{u}_s \quad \text{[A4]}$$

In the region where divergence-free condition applies ($\nabla \cdot \vec{u}_s = 0$), Eq. [A4] can be simplified as follows:

$$\vec{u}_s \cdot \nabla c_{\text{mix}} = -f_\ell \Delta \vec{u}_{\ell-s} \cdot \nabla c_\ell \quad \text{[A5]}$$

NOMENCLATURE

c_ℓ, c_s	species concentration
$c_{\ell,0}$	alloy composition applied at the inlet
c_ℓ^*, c_s^*	interface equilibrium species concentration
$C_{\ell s}^D$	species diffusive flux (kg m^{-3} s^{-1})
$C_{\ell s}^M$	species exchange due to phase change (kg m^{-3} s^{-1})
c_{mix}	mixture concentration
Δc_{mix}	deviation of c_{mix} in the solidified slab
c_p^ℓ, c_p^s	specific heat (J kg^{-1} K^{-1})
D_ℓ	diffusion coefficient (m^2 s^{-1})
d_c	diameter of columnar trunk (m)
f_ℓ, f_s	volume fraction
$f_{\ell,0}$	initial liquid fraction applied at the inlet
f_s^{cent}	solid volume fraction at centerline
$f_{s,\text{Start}}^{\text{cent}}$, $f_{s,\text{End}}^{\text{cent}}$	solid volume fraction of strand core at the start and end of soft reduction
$f_s^{0-\text{strength}}$	solid volume fraction of zero strength
$\vec{g}$	gravity (m s^{-2})
H^*	volume heat exchange rate between solid and liquid phases (W m^{-3} K^{-1})
h	heat transfer coefficient between strand and cooling media (W m^{-3} K^{-1})
h_ℓ, h_s	enthalpy (J kg^{-1})
h_ℓ^{ref}, h_s^{ref}	enthalpy at reference temperature (J kg^{-1})
Δh_f	latent heat (heat of fusion) (J kg^{-1})
K	permeability (m^2)
k	solute partition coefficient
k_ℓ, k_s	thermal conductivity (W m^{-1} K^{-1})
l	slab length (m)
l_B	distance between neighboring rolls (m)
l_{SR}	length of soft reduction segment (m)
$M_{\ell s}$	solidification mass transfer rate (kg s^{-1} m^{-3})
m	liquidus slope of the binary phase diagram (K/wt pct)
N	number of bulging roll pairs
p	pressure (Pa)
$Q_{\ell s}^D$	energy exchange by heat transfer (J m^{-3} s^{-1})
Q_ℓ^M, Q_s^M	energy source term due to phase change (J m^{-3} s^{-1})
R_c	radius of columnar trunk (m)
R_f	far field radius of columnar trunk (m)
S_A	columnar surface concentration (m^{-1})
T, T_ℓ, T_s	temperature [K (°C)]
T_0	inlet temperature [K (°C)]
T_{ref}	reference temperature for enthalpy definition [K (°C)]
T_w	temperature of cooling media [K (°C)]
t	time (seconds)
$\vec{U}_{\ell s}^D$	momentum change due to drag force (kg m^{-2} s^{-2})
$\vec{U}_{\ell s}^M$	momentum exchange due to phase change (kg m^{-2} s^{-2})
$u_{x,s}$, $u_{z,s}$	solid velocity in x- and z- component (m s^{-1})
$u_{x,s}^b$, $u_{z,s}^b$	strand surface velocity in x- and z- component (m s^{-1})
u_z^{IN}	outlet velocity of the calculation domain (m s^{-1})
$u_{z,s}^{\text{IN}}$, $u_{z,s}^{\text{OUT}}$	solid velocity at the entrance and exit of the soft-reduction segment (m s^{-1})
$\vec{u}_\ell$, $\vec{u}_s$	velocity vector (m s^{-1})
$\Delta \vec{u}_{\ell-s}$	relative velocity (m s^{-1})
$\Delta u_{x,\ell-s}$, $\Delta u_{z,\ell-s}$	x- and z-component of the relative velocity (m s^{-1})
v_{cast}	casting velocity ($i.e.$, the solid velocity of the entrance of the MSR segment) (m s^{-1})
v_{R_c}	columnar trunk growth velocity (m s^{-1})
w	thickness of slab (before soft reduction) (m)
z_0	starting position of bulging (m)
z_1, z_2	coordinates of start and end positions of soft-reduction segment (m)
δ or δ^b	magnitude of bulging (m)
$\delta_{\max}^b$	maximum amplitude of bulging (m)
ε	absolute soft-reduction amount (m)
Φ_{imp}	columnar growing surface impingement
ϕ_1, ϕ_2	empirical constants in Eq. [17]
γ	MSR factor (s^{-1})
λ_1	primary dendrite arm space of columnar (m)
ρ_ℓ, ρ_s	density (kg m^{-3})

ρ_{s+p} density of mixed solid and pores that are frozen in the interdendritic region (kg m^{-3})

μ_ℓ viscosity (kg m^{-1} s^{-1})

$\bar{\bar{\tau}}_{\ell s}$ stress–strain tensors (kg m^{-1} s^{-1})

SUBSCRIPTS

ℓ, mark liquid

S solid phases

REFERENCES

1. K. Schwerdtfeger: *Metallurgie des Stranggießens – Gießen und Erstarren von Stahl*, Verlag Stahleisen mbH, Düsseldorf, Germany, 1992.
2. R. Thome and K. Harste: *Steel Res. Int.*, 2004, vol. 75, pp. 693–700.
3. R. Thome and K. Harste: *ISIJ Int.*, 2006, vol. 46, pp. 1839–44.
4. H. Preßlinger, S. Ilie, P. Reisinger, A. Schiefermüller, A. Pissenberger, E. Parteder, and C. Bernhard: *ISIJ Int.*, 2006, vol. 46, pp. 1845–51.
5. S. Ilie, H. Preßlinger, A. Schiefermüller, A. Pissenberger, and P. Reisinger: *BHM*, 2007, vol. 172, pp. 227–327.
6. O. Bode, K. Schwerdtfeger, H.G. Geck, and F. Höfer: *Ironmaking Steelmaking*, 2008, vol. 25, pp. 137–40.
7. S. Ogibayashi, M. Kobayashi, M. Yamada, and T. Mukai: *ISIJ Int.*, 1991, vol. 31, pp. 1400–47.
8. S. Ilie, R. Fuchs, K. Etzelsdorfer, C. Chimani, and K. Mörwald: *6th European Conference on Continuous Casting*, Riccione, Italy, June 4–8, 2008.
9. C.H. Yim, J.K. Park, B.D. You, and S.M. Yang: *ISIJ Int.*, 1996, vol. 36, pp. 231–34.
10. R. Nyström and K.H. Spitzer: *Steel Res. Int.*, 2003, vol. 74, pp. 700–07.
11. K. Ayata, S. Koyama, H. Nakata, S. Kawasaki, K. Ebina, and T. Hata: *6th Int. Iron and Steel Cong.*, ISIJ, Tokyo, Japan, 1990, pp. 279–84.
12. K. Ebina, K. Fujii, S. Chimono, S. Toyoshima, and I. Takagi: *La Revue de Métallurgie CIT*, Grenoble, France, 1992, pp. 783–91.
13. A. Reichert, K.H. Tacke, K. Harste, M. Hecht, J. Heilemann, U. Ölmann, K. Schwerdtfeger, B. Barber, R.C. Beaverstock, and R. Walmsey: *ECSC Report EUR 20190*, European Commission, 2002, pp. 1–154.
14. S. Ogibayashi, M. Ushimura, K. Isobe, H. Maede, Y. Nishihara, and S. Sato: *6th Int. Iron and Steel Cong.*, ISIJ, Tokyo, Japan, 1990, pp. 271–78.
15. K. Isobe, Y. Kusano, S. Nogushi, K. Ishyama, A. Yamanaka, T. Horie, and M. Uehara: *Int. Symp. on Near-Net-Shape Casting in the Minimills*, University of British Columbia, Vancouver, Canada, 1995, pp. 179–82.
16. K. Miyazawa and K. Schwerdtfeger: *Arch. Eisenhüttenwes*, 1981, vol. 52, pp. 415–22.
17. T. Kajitani, J.-M. Drezet, and M. Rappaz: *Metall. Mater. Trans. A*, 2001, vol. 32A, pp. 1479–91.
18. F. Mayer, M. Wu, and A. Ludwig: *Proc. MCWASP XII*, S.L. Cockcroft and D.M. Maijer, eds., TMS, Warrendale, PA, 2009, pp. 279–86.
19. F. Mayer, M. Wu, and A. Ludwig: *Steel Res. Int.*, 2010, vol. 81, pp. 660–67.
20. A. Ludwig and M. Wu: *Mater. Sci. Eng. A*, 2005, vols. 413–414, pp. 109–14.
21. M. Wu and A. Ludwig: *Metall. Mater. Trans. A*, 2006, vol. 37A, pp. 1613–31.
22. M. Wu and A. Ludwig: *Metall. Mater. Trans. A*, 2007, vol. 38A, pp. 1465–75.
23. A. Ludwig, M. Grasser, M. Wu, A. Kuhn, and J. Riedle: *Int. J. Fluid Dynamics Mater. Proc.*, 2006, vol. 1, pp. 285–300.
24. R.B. Bird, W.E. Steward, and E.N. Lightfoot: *Transport Phenomena*, Wiley, New York, NY, 1960, pp. 196–200.
25. E. Niyama, T. Uchida, M. Morikawa, and S. Saito: *AFS Int. Cast Metals Res.*, 1981, vol. 6, pp. 16–22.
26. Fluent 6.3 User's Guide*:* Fluent Inc., Lebanon, NH, Sept. 2006.
27. S. Ogibayashi, R. Nishihara, and S. Satou: *Tetsu-to-Hagané*, 1997, vol. 83, pp. 36–41.
28. S. Luo, M. Zhu, C. Ji, Y. Yang, and J. Yang: *J. Univ. Sci. Techn. Beijing*, 2010, vol. 32, pp. 890–94.
29. A.K. Dahle and D.H. St. John: *Acta Mater.*, 1999, vol. 47, pp. 31–41.
30. H.F. Shen and C. Beckermann: *Metall. Mater. Trans. B*, 2002, vol. 33B, pp. 69–78.
31. L.C. Nicolli, A. Mo, and M. M'Hamdi: *Metall. Mater. Trans. A*, 2005, vol. 36A, pp. 433–42.
32. M. Bellet and V.D. Fachinotti: *Proc. MCWASP XI*, C-A. Gandin and M. Bellet, eds., TMS, Warrendale, PA, 2006, pp. 169–76.
33. V.D. Fachinotti, S.L. Corre, N. Triolet, M. Bobadilla, and M. Bellet: *Int. J. Numer. Meth. Eng.*, 2006, vol. 67, pp. 1341–84.